Robotics and Autonomous Systems 194 (2025) 105162

Contents lists available at ScienceDirect

Robotics and Autonomous Systems

journal homepage: www.elsevier.com/locate/robot

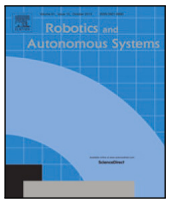

Control and stabilization of quadcopters subjected to propeller failures

Junio Santos Bulhões [a,b,d,*], Cristiane Lopes Martins [e], Viviane M. Gomes Pacheco [a,d,f], Alana da Silva Magalhães [d], Clóves Gonçalves Rodrigues [f], Antonio Paulo Coimbra [c], Wesley Pacheco Calixto [a,c,d,**]

[a] Electrical, Mechanical & Computer Engineering School, Federal University of Goias, Goiania, Goias, Brazil
[b] Federal Institute of Mato Grosso (IFMT), Mato Grosso, Brazil
[c] Institute of Systems and Robotics, Coimbra University, Coimbra, Portugal
[d] Technology Research and Development Center (GCITE), Federal Institute of Goias, Goiania, Goias, Brazil
[e] Federal University of Mato Grosso (UFMT), Mato Grosso, Brazil
[f] Graduate Program in Production and Systems Engineering, Pontifical Catholic University of Goias, Goiania, Goias PC 74605-010, Brazil

ARTICLE INFO

Dataset link: 10.24433/CO.3597880.v1

Keywords:
System modeling
Quadcopters
Propeller failure
Stabilization
Sliding mode control

ABSTRACT

This work develops an auxiliary control system based on sliding mode control in order to stabilize quadcopters in the event of propeller failures, a significant challenge in the operation of unmanned aircraft. The proposed approach includes the implementation of modern control techniques, extensively tested in both a nonlinear simulator and a testing platform, allowing the reproduction of scenarios with up to 30% power loss in one of the motors. The combination of detailed simulations and practical experiments demonstrates the efficiency of sliding mode control, which is able to mitigate the effects of failures by reducing deviations in the ϕ and θ angles by more than 80% at the initial moments and maintaining partial stability of the angle ψ. In addition to surpassing other approaches in terms of efficiency, the proposed method preserves the aircraft's autonomy, offering a robust and practical solution for application in real operational environments, ensuring greater safety and reliability in quadcopter control.

1. Introduction

With the advancement of automation, autonomous devices are increasingly replacing repetitive, dangerous, or hazardous tasks, with the aim of protecting human health and improving quality of life [1]. Among the most notable innovations are industrial robots, designed to perform specific activities in industrial environments, and autonomous vehicles, capable of operating and navigating without human intervention. Unmanned aerial vehicles (UAVs), commonly known as drones, stand out among these technologies. They are remotely controlled and used in various fields, such as mapping, infrastructure inspection, and delivery [2]. These aircraft, categorized into two groups based on their flight mode (fixed-wing and rotary-wing) [3], have seen significant advancements, with applications ranging from military use to commercial services [4].

Drones, which originated during the Cold War, are widely used in fields such as reconnaissance, object transport, journalism, fire prevention, environmental monitoring, and precision agriculture, replacing conventional methods in several tasks [5–11]. However, their high acquisition and maintenance costs limit their adoption in certain areas [12], and losses due to crashes, sensor damage, and electrical failures are common [13]. Such failures can compromise drone stabilization, particularly if the conventional control system cannot manage the resulting dynamic changes [14], leading to financial losses and posing physical risks to people and animals [15]. In critical situations, such as organ transport, drone loss can have severe consequences, which requires increased safety measures [16].

Several strategies have been proposed to mitigate the impact of rotor failures during flight, including fault-tolerant systems with parachutes [17] and adaptive controls that maintain stability in octocopters even when a single rotor fails [18,19]. Zeghlache et al. [20] developed algorithms based on fuzzy logic and neural networks to control octocopters with rotor failures, while Santos et al. [21] applied PID control to hexacopters, reducing the impact of crashes, although failing to prevent rotation around the z-axis. Nguyen et al. [22] used sliding mode control (SMC) for stabilization, and Mazeh & Sahili [23] tuned PID parameters using particle swarm optimization. In quadcopters, Mueller & D'Andrea [24] and Morozov [25] used the linear quadratic

* Corresponding author.
** Corresponding author at: Electrical, Mechanical & Computer Engineering School, Federal University of Goias, Goiania, Goias, Brazil.
E-mail addresses: junio.bulhoes@ifmt.edu.br (J.S. Bulhões), wesley.pacheco@ufg.br (W.P. Calixto).

https://doi.org/10.1016/j.robot.2025.105162
Received 5 September 2024; Received in revised form 14 June 2025; Accepted 6 August 2025
Available online 16 August 2025

Table 1
Synthesis of studies that addresses rotor failures.

Papers	Year	Number of actuators	Control technique	Optimization process
Mueller and D'Andrea [24]	2014	4	LQR	No
Merheb et al. [30]	2014	4	SMC	Yes
Santos et al. [21]	2015	6	PID	No
Wang and Zhang [18]	2017	8	Adaptive control	No
Lee et al. [19]	2018	8	Adaptive control	No
Zeghlache et al. [20]	2018	8	FUZZY and ANN	Yes
Morozov [25]	2018	4	LQR	Yes
Nguyen and Hong [29]	2019	4	PID	No
Wu et al. [26]	2019	4	SMC	Yes
Mazeh and Sahili [23]	2019	6	PID	Yes
Nguyen et al. [22]	2019	6	SMC	Yes
Baldini et al. [28]	2020	4	OCA	Yes
Jung and Bang [27]	2021	4	Predictive control	Yes

regulator (LQR) to stabilize despite rotor failures, while Wu et al. [26] sacrificed yaw control around the z axis to maintain vehicle stability.

Jung & Bang [27] developed a computational model that applies predictive control to adjust the parameters of the quadcopter, stabilizing the vehicle when the speed of a faulty rotor approaches nominal levels. Baldini et al. [28] used the optimal control allocation (OCA) technique to reconfigure the quadcopter model, mitigating the effects of propulsor power loss on flight dynamics. Nguyen & Hong [29] integrated PID control with rotor fault diagnosis in their model. Merheb et al. [30] simulated the shifting of the quadcopter's center of mass to enable it to operate as a tricopter during flight. Table 1 presents these studies chronologically, facilitating the analysis of the number of actuators, control techniques, and optimization of the controller parameters used.

The studies summarized in Table 1 address the challenge of thruster failures in unmanned aerial vehicles, highlighting that as the number of thrusters decreases, the complexity of the problem increases. Stabilizing quadcopters during failures, given their dynamics and the limited number of actuators, remains an underexplored area. Except for the theoretical work performed by Merheb et al. [30], which proposes to change the center of mass in order to control the quadcopter as a tricopter, none of the studies mentioned validates their simulation results through practical experiments. This highlights a gap in the development of control techniques to manage rotor failures in quadcopters, ensuring equipment and payload integrity without compromising autonomy or increasing system mass.

This work is justified by the proposal to investigate control techniques for stabilizing quadcopters in the event of power loss in one of the rotors. Based on this identified gap, the primary hypothesis is formulated: If the failure of one engine occurs gradually and the remaining three provide sufficient thrust to compensate for it, control techniques can be used to stabilize the quadcopter, thereby preventing its loss of lift.

The primary objective of this work is to develop an auxiliary control system for quadcopters that operates during thruster failures, aiming to prevent material damage and ensure safety within the device's operational area. Specifically, the objectives include: (i) designing a three-dimensional test platform model, (ii) building the test platform prototype according to this model, (iii) developing a simulator based on the mathematical model of the quadcopter, (iv) integrating and developing the control system within the simulator, (v) validating the implemented test platform, (vi) analyzing scenarios of gradual failures in the thruster using the test platform, and (vii) proposing an auxiliary control system to mitigate the effects of failures and validating this system based on the results of the test platform.

This work stands out for its originality in developing an auxiliary control system that stabilizes quadcopters during rotor failures without adding extra weight, thus preserving flight autonomy. The novelty lies in the redistributing of the lift force among the three remaining thrusters, minimizing the impact of power loss. The significance of this study is its ability to offer a computationally efficient safety solution that can be easily applied to any quadcopter without requiring structural modifications, simply by adjusting the existing control algorithm. The structure of this work is as: Section 2 covers the theoretical foundations, including the expressions governing the rotational movements of the quadcopter. Next, Section 3 describes the proposed methodology for the development of the auxiliary control system, including testing and validation. Section 4 presents the results obtained from applying the methodology. Finally, Section 6 concludes the work.

2. Theoretical background

This section presents the concepts and mathematical expressions that underlie the motion of quadcopters, focusing on the generic model, the dynamics of the vehicle and the forces and torques involved. These elements, including aerodynamic forces and motor torques, are necessary for developing control strategies that ensure stability and maneuverability. Furthermore, the principles of sliding mode control and system stability according to Lyapunov's theory are discussed.

2.1. Quadcopter dynamics and its generic model

According to Bhargavapuri et al. [31], the mathematical model of the quadcopter in the configuration of the + axis establishes the relationship between the angular velocities p, q and r and the body frame of the quadcopter $\mathcal{F}_b$. In this context, p corresponds to the angular velocity around the $\hat{i}_b$ axis, q around the $\hat{j}_b$ axis and r around the $\hat{k}_b$ axis. However, each angle is defined within a specific coordinate system [32,33]. As discussed by Stevens et al. [34], the first-order time derivatives of the orientation angles ϕ, θ, and ψ, denoted by $\dot{\phi}$, $\dot{\theta}$, and $\dot{\psi}$, respectively, can be correlated to the angular velocities p, q, and r following the previously adopted rotation sequence. This correlation is presented in (1), from which the relationship between angular velocities p, q and r can be described in matrix form, as given in (2) [32].

$$\begin{aligned}
\dot{\phi} &= p + q\sin(\phi)\tan(\theta) + r\cos(\phi)\tan(\theta),\\
\dot{\theta} &= q\cos(\phi) - r\sin(\phi),\\
\dot{\psi} &= q\frac{\sin(\phi)}{\cos(\theta)} + r\frac{\cos(\phi)}{\cos(\theta)}.
\end{aligned} \tag{1}$$

$$\begin{bmatrix}\dot{\phi}\\ \dot{\theta}\\ \dot{\psi}\end{bmatrix} = \begin{bmatrix}1 & \sin\phi\tan\theta & \cos\phi\tan\theta\\ 0 & \cos\phi & -\sin\phi\\ 0 & \sin\phi\sec\theta & \cos\phi\sec\theta\end{bmatrix}\cdot\begin{bmatrix}p\\ q\\ r\end{bmatrix} \tag{2}$$

Based on Newton's second law, the time rate of change in linear momentum $\boldsymbol{h}_i$ is related to the torque $\boldsymbol{\tau}_i$ of the system, both defined in the inertial frame $\mathcal{F}_i$, as given by (3) [35]. The analysis of angular momentum follows a similar approach to that of linear momentum. Therefore, (3) must be reformulated when transitioning from the inertial frame $\mathcal{F}_i$ to the body-fixed frame $\mathcal{F}_b$, taking into account the Coriolis

inertial force.[1] This results in (3) and (4), where $\boldsymbol{h}_b$ represents the angular momentum vector and $\boldsymbol{\tau}_b$ the torque vector on the quadcopter due to the propellers, both defined in the body-fixed frame of the quadcopter $\mathcal{F}_b$ [34]. The angular momentum $\boldsymbol{h}_b$ in frame $\mathcal{F}_b$ is expressed as $\boldsymbol{J}\boldsymbol{\omega}_{b/i}$, where $\boldsymbol{J}$ is the inertia matrix and $\boldsymbol{\omega}_{b/i}$ is the angular velocity vector in frame $\mathcal{F}_b$ [34,36]. To solve the expression (4), the Euler equations for rigid bodies are used [35], as given by (5).

$$\dot{\boldsymbol{h}}_i = \boldsymbol{\tau}_i \tag{3}$$

$$\dot{\boldsymbol{h}}_b + \boldsymbol{\omega}_{b/i} \times \boldsymbol{h}_b = \boldsymbol{\tau}_b \tag{4}$$

$$\boldsymbol{J}\dot{\boldsymbol{\omega}}_{b/i} = -\boldsymbol{\omega}_{b/i} \times \boldsymbol{J}\boldsymbol{\omega}_{b/i} + \boldsymbol{\tau}_b \tag{5}$$

According to Kleppner & Kolenkow [35], when the reference frame $\mathcal{F}_b$ is fixed at the center of mass of the quadcopter and the mass distribution is symmetric, the inertia matrix $\boldsymbol{J}$ becomes diagonal, with J_x, J_y, and J_z corresponding to the principal moments of inertia relative to the X_b, Y_b, and Z_b axes, respectively. When the X_b and Y_b axes are aligned with the arms of the quadcopter, the matrix $\boldsymbol{J}$ becomes symmetric and J_x and J_y are equal [37,38]. Considering $\boldsymbol{\omega}_{b/i} = [p, q, r]^{\mathrm{T}}$, (5) can be rewritten in matrix form by isolating the term $\dot{\boldsymbol{\omega}}_{b/i}$. Applying the inverse of $\boldsymbol{J}$ and computing the cross product $\boldsymbol{\omega}_{b/i} \times \boldsymbol{J}\boldsymbol{\omega}_{b/i}$, the expression (6) is derived, where τ_ϕ, τ_θ, and τ_ψ represent the torques applied to the quadcopter [39]. This expression describes the dynamic behavior of the quadcopter with three degrees of freedom (3DOF) and the three rotational movements that it performs [31].

$$\begin{bmatrix} \dot{p} \\ \dot{q} \\ \dot{r} \end{bmatrix} = \begin{bmatrix} \frac{(J_y - J_z)\cdot qr}{J_x} \\ \frac{(J_z - J_x)\cdot rp}{J_y} \\ \frac{(J_x - J_y)\cdot pq}{J_z} \end{bmatrix} + \begin{bmatrix} \frac{\tau_\phi}{J_x} \\ \frac{\tau_\theta}{J_y} \\ \frac{\tau_\psi}{J_z} \end{bmatrix} \tag{6}$$

2.2. Forces and torques applied to quadcopters

The quadcopter propulsion systems consist of three main components: (i) propellers, (ii) motors, and (iii) speed controllers. Various types of motor, particularly direct current (DC) motors, are used to generate the necessary thrust for the propellers [40]. Among the most commonly used motors in quadcopters are brushless direct current (BLDC) motors, which are powered by low-voltage inverters with trapezoidal waveforms [41]. Each of the four motors is individually controlled by an electronic speed controller (ESC), although a single ESC can be used to control all motors simultaneously [42]. The role of the ESC is to convert the direct current from the battery into a trapezoidal direct current with variable frequency and amplitude, which supplies it to the motors [43].

Fig. 1, adapted from Nekoukar & Dehkordi [44], illustrates the top view of the quadcopter, highlighting the arrangement of the motors in the propulsion system. Among the four BLDC motors, M_2 and M_4 rotate clockwise, while M_1 and M_3 rotate counterclockwise. The torque vector generated by these motors is given by (7) [32,45]. The torque τ_ϕ is generated by the difference in thrust between motors M_2 and M_4, while the torque τ_θ results from the difference in thrust between motors M_1 and M_3. The torque τ_ψ, on the other hand, is influenced by the combined effect of all four motors, depending on their rotation directions. The torque τ_ϕ controls the roll motion and the torque τ_θ controls the pitch motion, both responsible for tilting the quadcopter and allowing translational movements. Finally, the torque τ_ψ regulates the yaw motion, adjusting the orientation of the propellers and allowing the quadcopter's arms to rotate around its center.

[1] The Coriolis inertial force, or Coriolis pseudoforce, is not a force in the traditional sense; it is perceived only by observers in non-inertial frames rotating relative to the inertial frame, particularly when moving toward or away from the center of rotation.

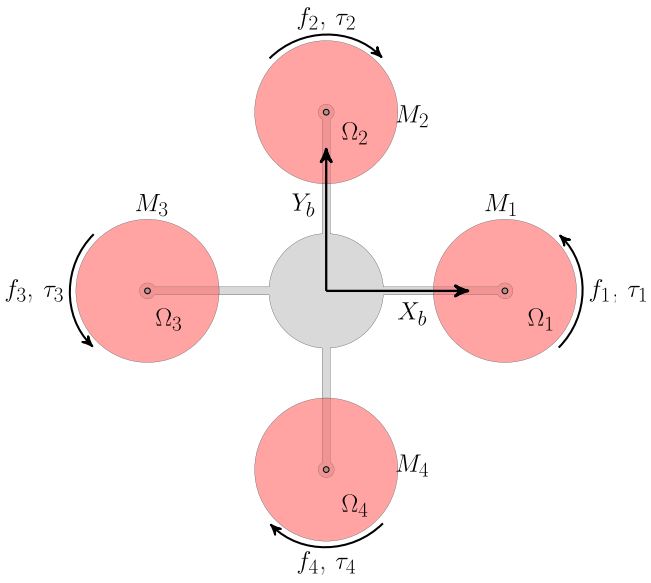

Fig. 1. Definition of rotational direction of each motor on the quadcopter.

$$\begin{bmatrix} \tau_\phi \\ \tau_\theta \\ \tau_\psi \end{bmatrix} = \begin{bmatrix} 0 & l_b & 0 & -l_b \\ -l_b & 0 & l_b & 0 \\ -k_\psi & k_\psi & -k_\psi & k_\psi \end{bmatrix} \cdot \begin{bmatrix} f_1 \\ f_2 \\ f_3 \\ f_4 \end{bmatrix} \tag{7}$$

2.3. Sliding mode control in nonlinear systems

Nonlinear systems, such as quadcopters, can exhibit unexpected behaviors due to parametric uncertainties or the simplification of the nonlinear model during analysis [46]. According to Herrera et al. [47], sliding mode control (SMC) is an effective technique for designing controllers for both linear and nonlinear systems, and it is widely used in various fields, such as electronics, robotics, and chemical processes. SMC applies a control law that drives the system error $e(t)$ and its derivative $\dot{e}(t)$ to the sliding surface. Once these states reach the surface, any disturbance that deviates the system from it is quickly corrected by the switching process [48].

Ahmad et al. [49] explain that the design of SMC controllers can be divided into two phases: (i) selecting the sliding surface and (ii) implementing the control law that keeps the state variables on the sliding surface. Thus, the first step in the SMC design is the selection of the sliding surface s. The expression (8) represents the sliding surface, consisting of a first-order linear differential equation, where λ represents its eigenvalue [50]. Furthermore, the time derivative of (8) yields (9).

$$s = \lambda e(t) + \dot{e}(t) \tag{8}$$

$$\dot{s} = \lambda \dot{e}(t) + \ddot{e}(t) \tag{9}$$

After selecting the sliding surface, the next step is to implement the control law that drives the system states toward the equilibrium region. According to Ahmad et al. [49], expression (10) is considered a robust control rule, where the sign function $\mathtt{snl}(x)$ is defined as -1 for $x < 0$, 0 for $x = 0$, and 1 for $x > 0$. In (10), k_1 and k_2 are constants, with k_1 controlling the sliding position and k_2 regulating the switching amplitude once the system reaches the sliding surface [50].

$$\dot{s} = -k_1 s - k_2 \mathtt{snl}(s) \tag{10}$$

Fig. 2, adapted from Vaidyanathan & Lien [48], illustrates the phase plane of the system represented in the state space, where $x_1(t) = e(t)$

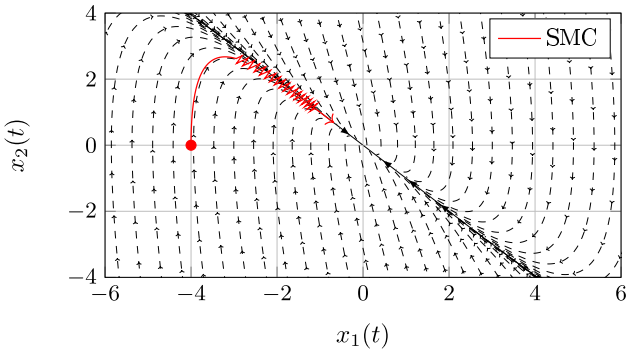

Fig. 2. Phase plan.

and $x_2 = \dot{x}_1(t)$. The red curve presents the system behavior from a specific initial condition, $x_1(0) = -4$ and $x_2(0) = 0$. In this scenario, the SMC guides the states toward the sliding region, where they remain confined, continuously corrected by the switching process until they reach the equilibrium point at (0,0).

Ullah et al. [51] state that the stability of the system can be analyzed using Lyapunov's theory, which checks whether the states converge to the equilibrium point $e(t) = 0$ and $\dot{e}(t) = 0$. Lyapunov's theory applies to systems of the type $\dot{x} = f(x)$ with an equilibrium point at $x = 0$. The function $\mathcal{V}(x)$ is considered a candidate Lyapunov function, and the system is considered stable in the Lyapunov sense if: (i) $\mathcal{V}(x) = 0$ if and only if $x = 0$, (ii) $\mathcal{V}(x) > 0$ for all $x \neq 0$, (iii) $\dot{\mathcal{V}}(x) \leq 0$, ensuring the system is locally stable, and (iv) $\dot{\mathcal{V}}(x) < 0$ for all $x \neq 0$, which implies that the system is asymptotically stable. According to Wu et al. [26], assuming the Lyapunov candidate function as in (11), this function is always greater than or equal to zero, and its derivative is given by (10). Therefore, for the system under sliding mode control to be considered asymptotically stable, $\dot{\mathcal{V}}(s)$ must always be negative.

$$\mathcal{V}(s) = \frac{s^2}{2} \tag{11}$$

$$\dot{\mathcal{V}}(s) = \dot{s}s \tag{12}$$

3. Methodology

This section describes the methodology for developing and validating the auxiliary control system that reduces power in quadcopter motors. The failure scenarios are defined, and the angles during failures are collected and analyzed. Then a sliding mode control is developed to stabilize the system. Finally, the control is tested and validated through simulations and experiments to ensure its efficiency and reliability.

3.1. Auxiliary control for quadcopter stability

Quadcopters face stability challenges during electrical failures in their propellers, which can lead to crashes and damage. Solutions such as parachutes can mitigate these risks but reduce autonomy. This methodology proposes an auxiliary control system that replaces current control after detecting a power loss in a propeller, redistributing control efforts to stabilize the angles ϕ, θ, and ψ, enabling safe landing. The system is evaluated using sliding mode control (SMC), with simulations and bench tests to optimize performance and avoid destructive tests. Fig. 3 illustrates the proposed methodology, divided into five main tasks: (i) selecting the test platform, (ii) defining the simulation for the failure, (iii) executing the failure on the platform and analyzing the results, (iv) developing the auxiliary SMC control, and (v) validating the auxiliary control system using SMC.

The test platform should provide a controlled environment that allows the quadcopter to perform rotational movements with minimal interference in its dynamics, while maintaining the center of mass in a fixed position. The methodology illustrated in Fig. 3 follows a flow that, after validating the test platform, focuses on developing the auxiliary control system. This process involves four main stages: first, failure scenarios are defined to simulate adverse conditions of power loss in the propeller. Then tests are conducted on the platform, where data on the behavior of the angles are collected and analyzed. The third stage involves developing the auxiliary control system using SMC, which is tested in a nonlinear simulator. Finally, the proposed control system is validated again on the platform, ensuring its efficiency and functionality under real conditions.

3.2. Definition of failure scenarios

In real-world scenarios, quadcopter failures can occur due to external factors, such as collisions with birds or trees, or internal factors, such as overheating of the speed controller's power converter. In this study, power loss in a propeller is artificially simulated by reducing its speed, a task carried out by a specifically developed algorithm. The failure algorithm is activated when the control system (CR) is operating and the angles ϕ, θ, and ψ are stabilized. The algorithm development requires several configurations: (i) identifying which propeller will experience the failure, (ii) defining the failure initiation time, and (iii) determining the magnitude of the failure. The choice of propeller is arbitrary and does not affect the study since the quadcopter is symmetrical, ensuring consistent results regardless of the selected propeller.

After the propeller is selected to simulate the failure scenario, it is used consistently across all experiments to standardize the results and facilitate the analysis of its effects on the quadcopter's dynamics. The timing of initiation of the failure is then determined. The failure time t_F is defined as the interval between the activation of the PID control system (current control) and the activation of the failure algorithm. Fig. 4 hypothetically illustrates the speed of the affected propeller, which is reduced t_F seconds after the control system is activated, initiating the failure algorithm and marking the beginning of the failure region (FR).

Fig. 4 illustrates the control region CR and the failure region FR. After selecting the propeller and determining the failure time, the next step is to define the magnitude of the failure M_F, which controls the percentage reduction in thrust of the chosen propeller. A reduction of M_F in the original thrust of the propeller results in a decrease of $2M_F - M_F^2$ in its original speed. The range analyzed is given by $M_F = [0\% : p_{ss}\% : M_{F_{max}}\%]$, where p_{ss} is the interval step. In Fig. 4, the green curve in the FR region represents the propeller speed with a failure magnitude of $M_F = 10\%$, while the blue dotted line indicates the expected propeller speed without failure. The parameter $M_{F_{max}}$ is determined experimentally and defines the threshold beyond which the effects of power loss can be reversed, allowing the quadcopter to stabilize.

With the propulsion system selected, tests are conducted to observe the quadcopter's behavior in response to power loss in one of the propellers. The fault simulation algorithm is implemented in the quadcopter's controller, enabling controlled experiments. Each scenario, varying the failure factor M_F, is analyzed to examine its effects on the angles ϕ, θ, ψ, and the stability of the quadcopter. To standardize the experiments and facilitate comparison across different scenarios, the initial conditions ϕ_i, θ_i, and ψ_i are manually set to be similar at the moment the PID control system is activated. This ensures uniformity in the results and allows for a detailed analysis of angle variations as the magnitude of the failure increases. Furthermore, empirical tests are necessary to determine $M_{F_{max}}$, the point at which the system becomes unstable for at least one of the angles. The value of M_F gradually increases in preliminary tests until the instability is identified.

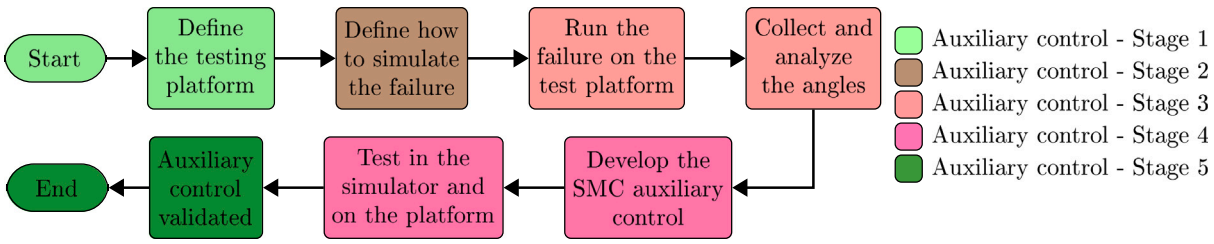

Fig. 3. Flowchart of the proposed methodology.

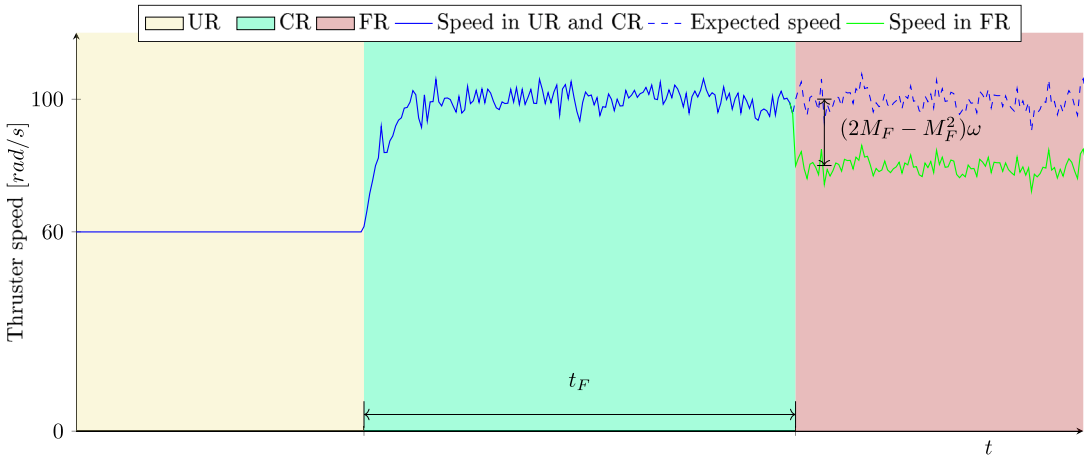

Fig. 4. Hypothetical representation of thruster speed that has a failure with $M_F = 10\%$. (For interpretation of the references to color in this figure legend, the reader is referred to the web version of this article.)

3.3. Stability, convergence, and resilience in attitude control

Following the definition of the failure scenarios considered, it becomes necessary to formally evaluate the stability of the control system under partial loss of propulsion. In this context, a theoretical analysis is developed using a specific Lyapunov function capable of representing the complete nonlinear dynamics of the quadcopter, including the couplings among the roll ϕ, pitch θ and yaw ψ axes, even under adverse conditions. The vector of error in angular velocity is defined as $\tilde{\boldsymbol{\omega}} = \boldsymbol{\omega}_d - \boldsymbol{\omega}$, where $\boldsymbol{\omega} = [p, q, r]^T$ denotes the actual angular velocities and $\boldsymbol{\omega}_d$ the reference values. Similarly, the attitude error vector is defined as $\tilde{\boldsymbol{\varphi}} = \boldsymbol{\varphi}_d - \boldsymbol{\varphi}$, with $\boldsymbol{\varphi} = [\phi, \theta, \psi]^T$ representing the actual attitude angles and $\boldsymbol{\varphi}_d$ the desired values. The Lyapunov candidate function adopted is given by (13), where J is the diagonal inertia matrix and $k_\varphi > 0$ is the control gain. The function $\mathcal{V}$ is positive definite with respect to the tracking errors.

$$\mathcal{V}(\tilde{\boldsymbol{\omega}}, \tilde{\boldsymbol{\varphi}}) = \frac{1}{2}\tilde{\boldsymbol{\omega}}^T J \tilde{\boldsymbol{\omega}} + \frac{1}{2}k_\varphi \tilde{\boldsymbol{\varphi}}^T \tilde{\boldsymbol{\varphi}} \tag{13}$$

The time derivative of (13) is given by (14), considering the full rotational dynamics of the quadcopter as described in (15), where $\boldsymbol{\tau}$ denotes the control torques and $\boldsymbol{\Delta\tau}$ accounts for external disturbances and uncertainties, such as asymmetries and partial actuator failures. To mitigate the chattering phenomenon, the sign operator is replaced by a saturation function, defined in (16). Consequently, the sliding mode control law is defined by (17).

$$\dot{\mathcal{V}} = \tilde{\boldsymbol{\omega}}^T J \dot{\tilde{\boldsymbol{\omega}}} + k_\varphi \tilde{\boldsymbol{\varphi}}^T \dot{\tilde{\boldsymbol{\varphi}}} \tag{14}$$

$$J\dot{\boldsymbol{\omega}} + \boldsymbol{\omega} \times (J\boldsymbol{\omega}) = \boldsymbol{\tau} + \boldsymbol{\Delta\tau} \tag{15}$$

$$\text{sat}(s/\rho) = \begin{cases} 1 & \text{se} s/\rho > 1 \\ s/\rho & \text{se } |s/\rho| \le 1 \\ -1 & \text{se } s/\rho < -1 \end{cases} \tag{16}$$

$$\boldsymbol{\tau} = J(\dot{\boldsymbol{\omega}}_d - \lambda\tilde{\boldsymbol{\omega}} - k_s \,\text{sat}(s/\rho)) + \boldsymbol{\omega} \times (J\boldsymbol{\omega}) \tag{17}$$

By substituting (14) into (17), one obtains (18). Assuming that $|\boldsymbol{\Delta\tau}| \le \delta_\tau$ and applying Young-type inequalities to the last two terms of (18), inequalities (19) and (20) are derived, where $\epsilon_1, \epsilon_2 > 0$ are arbitrary constants. Consequently, the derivative of $\mathcal{V}$ can be upper-bounded as shown in (21). Through algebraic manipulation and the redefinition of ξ and ϵ, one obtains (22) and, finally, (23). This result ensures global asymptotic stability in the Lyapunov sense, provided that $\xi > 0$, which can be guaranteed by an appropriate selection of ϵ_1, ϵ_2, and the controller gains.

$$\dot{\mathcal{V}} = -\lambda\tilde{\boldsymbol{\omega}}^T J\tilde{\boldsymbol{\omega}} - k_s\tilde{\boldsymbol{\omega}}^T J \,\text{sat}(s/\rho) + \tilde{\boldsymbol{\omega}}^T\boldsymbol{\Delta\tau} + k_\varphi\tilde{\boldsymbol{\varphi}}^T\tilde{\boldsymbol{\omega}} \tag{18}$$

$$\tilde{\boldsymbol{\omega}}^T\boldsymbol{\Delta\tau} \le \frac{1}{2\epsilon_1}\|\tilde{\boldsymbol{\omega}}\|^2 + \frac{\epsilon_1}{2}\|\boldsymbol{\Delta\tau}\|^2, \tag{19}$$

$$k_\psi\tilde{\boldsymbol{\varphi}}^T\tilde{\boldsymbol{\omega}} \le \frac{1}{2\epsilon_2}\|\tilde{\boldsymbol{\omega}}\|^2 + \frac{\epsilon_2}{2}k_\varphi^2\|\tilde{\boldsymbol{\varphi}}\|^2, \tag{20}$$

$$\dot{\mathcal{V}} \le -\lambda\|\tilde{\boldsymbol{\omega}}\|^2 + \frac{1}{2\epsilon_1}\|\tilde{\boldsymbol{\omega}}\|^2 + \frac{1}{2\epsilon_2}\|\tilde{\boldsymbol{\omega}}\|^2 + \frac{\epsilon_1}{2}\delta_\tau^2 + \frac{\epsilon_2}{2}k_\varphi^2\|\tilde{\boldsymbol{\varphi}}\|^2 \tag{21}$$

$$\xi = \lambda - \left(\frac{1}{2\epsilon_1} + \frac{1}{2\epsilon_2}\right), \quad \epsilon = \frac{\epsilon_1}{2}\delta_\tau^2 + \frac{\epsilon_2}{2}k_\varphi^2\|\tilde{\boldsymbol{\varphi}}\|^2, \tag{22}$$

$$\dot{\mathcal{V}} \le -\xi\|\tilde{\boldsymbol{\omega}}\|^2 + \epsilon \tag{23}$$

To ensure that the system reaches the sliding surface $s = \dot{e} + \lambda e = 0$ in finite time, the condition given by (24) is assumed, with $k_s > 0$ and $s(t)$ being Lipschitz continuous. Under these conditions, convergence occurs within a finite time. The maximum time t_s required to reach the sliding surface is bounded by (26). This result enables a direct estimate of the response time of the system as a function of the design parameters. In the context of this work, k_s can be expressed as a function of the gains k_1 and k_2 used in the implementation of adaptive control. The saturation function defined in (16) smooths the control action near the

sliding surface and mitigates high-frequency oscillations, thus enhancing the feasibility of real actuators. Consequently, the simulations to be performed are not expected to exhibit abrupt torque fluctuations, indicating that chattering will be effectively reduced.

$$\dot{\mathcal{V}} \leq -k_s \|s\| \tag{24}$$

$$t_s \leq \frac{\|s(0)\|}{k_s} \tag{25}$$

Finally, considering the presence of bounded external disturbances, such as wind gusts or sensor noise, it is assumed that $|\Delta\tau(t)| \leq \delta$, with δ being finite. Under this assumption, the derivative of the Lyapunov function can be bounded as in (26). Applying the Young-type inequality once again, the inequality (27) is obtained, with $\delta' > 0$. This result ensures that, although the system is not strictly asymptotically stable, it remains uniformly bounded, as expressed in (28). Therefore, even in the presence of finite-magnitude disturbances, the attitude errors remain confined within a neighborhood of the equilibrium point. This property formalizes the resilience of the system, reinforcing the practical applicability of the proposed controller in real-world scenarios.

$$\dot{\mathcal{V}} \leq -\xi \|\tilde{\omega}\|^2 + \delta \|\tilde{\omega}\| \tag{26}$$

$$\dot{\mathcal{V}} \leq -\xi \mathcal{V} + \delta' \tag{27}$$

$$\limsup_{t \to \infty} \mathcal{V}(t) \leq \frac{\delta'}{\xi} \tag{28}$$

3.4. Angle collection and analysis during failures

The tests conducted on the quadcopter generate data that are collected and stored for analysis. Primary data include angles ϕ, θ, ψ, and signals transmitted by the controller to the four electronic speed controllers (ESC): S_{M1}, S_{M2}, S_{M3}, and S_{M4}. The timestamp of each sample is important for constructing time series. After collection, the controller collects C_n samples of each variable and transmits them wirelessly to the server, following a client/server architecture in which the controller acts as the client and the software on the computer as the server. This software stores all data in a MySQL database, facilitating data retrieval, use, and manipulation to extract the necessary information. In the analysis of results, the simulator is adapted and fed the mathematical model, using the initial values from the experiments ϕ_i, θ_i, ψ_i, the control start time t_i, and the moment when failure occurs $t_i + t_F$.

This procedure aims to verify whether the developed nonlinear simulator can accurately reproduce the dynamic behavior of the quadcopter during a propeller failure. The simulator results are compared with the data collected from the test platform to assess its accuracy in representing the quadcopter in failure scenarios. For this analysis, the mean square difference $D_{MQ_{(\phi),(\theta),(\psi)}}$ given by (29) and the quadratic percentage error $E_{Q_{(\phi),(\theta),(\psi)}}$ given by (30) are used. In expression (29), $e_{(\phi),(\theta),(\psi)}(i)$ represents the error of the ith sample in the time series, i_0 is the first sample after the onset of the failure and N is the total number of samples. This metric is chosen because it penalizes systems with larger amplitude errors.

$$D_{MQ_{(\phi),(\theta),(\psi)}} = \sqrt{\frac{1}{N - i_0} \sum_{i=i_0}^{N} \left(e_{(\phi)(\theta)(\psi)}(i)\right)^2} \tag{29}$$

$$E_{Q_{(\phi),(\theta),(\psi)}} = \left| \frac{V_{NQ_s(\phi),(\theta),(\psi)} - V_{NQ_p(\phi),(\theta),(\psi)}}{V_{NQ_s(\phi),(\theta),(\psi)}} \right| \tag{30}$$

Expression (30) calculates the percentage deviation between the normalized angles obtained in the simulation $V_{NQ_s(\phi),(\theta),(\psi)}$ and those from the platform experiment $V_{NQ_p(\phi),(\theta),(\psi)}$. This expression allows for measuring individual deviations E_{Q_ϕ}, E_{Q_θ}, and E_{Q_ψ}. Data normalization is performed using expression (31), where $\min(\phi),(\theta),(\psi)$ represent the individual minimum values of the angles, $\max(\phi),(\theta),(\psi)$ represent the maximum values, and $V_{NQ_{(\phi),(\theta),(\psi)}}$ are the normalized values within the range [0, 1].

Table 2
Parameters required for the implementation of the proposed SMC controller.

Angle	Error	Lyapunov		
	$e(t)$	λ	k_1	k_2
ϕ	$e_\phi = \phi_d - \phi$	λ_ϕ	k_{1_ϕ}	k_{2_ϕ}
θ	$e_\theta = \theta_d - \theta$	λ_θ	k_{1_θ}	k_{2_θ}
ψ	$e_\psi = \psi_d - \psi$	λ_ψ	k_{1_ψ}	k_{2_ψ}

$$V_{NQ_{(\phi),(\theta),(\psi)}} = \frac{D_{MQ_{(\phi),(\theta),(\psi)}} - \min(\phi),(\theta),(\psi)}{\max(\phi),(\theta),(\psi) - \min(\phi),(\theta),(\psi)} \tag{31}$$

With the angles normalized between [0, 1], the global mean square percentage error $E_{q_{global}}$ is calculated as the average of $E_{Q_{(\phi),(\theta),(\psi)}}$ for the angles ϕ, θ, and ψ. The parameter κ_q is defined as the acceptable threshold for variation between the simulator and the results of the platform to consider the validation successful. If $E_{q_{global}}$ is less than κ_q, the auxiliary control algorithm can be developed and tested in the simulator before implementation on the test platform, accelerating the development process by allowing multiple experiments to be carried out in less time. Finally, an auxiliary control algorithm is proposed to mitigate the negative impacts of power loss in the failed propeller, allowing the quadcopter to partially restore its rotational angles.

3.5. Development of the auxiliary control system

The proposed methodology aims to analyze and address failures that result in forces less than $1 - M_F$ of the expected propeller force and is applicable only in scenarios where a propeller cannot be completely shut down. However, failures that result in complete power failure typically exhibit prior symptoms. Therefore, the approach focuses on the early stages of such failures, allowing equipment control. When a failure is detected, the auxiliary control system immediately activates, with the aim of responding quickly enough for the controller to identify the propeller issue and implement preventive measures.

The controller replaces the PID control algorithm with the SMC algorithm to mitigate control efforts on the faulty propeller, adapting the quadcopter to the new failure scenario. The interval between the onset of the failure and its detection for the control switch is called Δ_d. From this point on, the auxiliary control system takes over and this phase is termed the region with active auxiliary control (ACR). Sliding mode control (SMC) is proposed to reduce the effects of failure, particularly on the angles ϕ and θ, which are important for stabilizing the quadcopter. The SMC is implemented independently, taking into account the effects observed on ϕ, θ, and ψ.

The control law used is given by (10), where the parameters λ, k_1, and k_2 are selected according to Lyapunov's theory, ensuring the asymptotic stability of the system. Table 2 lists the SMC parameters for the individual control of each angle. The error signal $e(t)$ for each angle is defined as the difference between the desired value and the value measured by the sensor. Thus, three sliding surfaces $S_{d\phi}$, $S_{d\theta}$, and $S_{d\psi}$ are used in the SMC, as defined in (8). Based on the expressions (6), (9), and (10), the necessary torques to stabilize the angles of the system are determined: torque τ_ϕ given by (32), torque τ_θ in (33) and torque τ_ψ given by (34).

$$\tau_\phi = -(J_y - J_z)\dot{\theta}\dot{\psi} + J_x\ddot{\phi}_d + J_x(\lambda_\phi + k_{1_\phi})\dot{e}_\phi + J_x\lambda_\phi k_{1_\phi} e_\phi + J_x k_{2_\phi} \mathrm{snl}(s_\phi) \tag{32}$$

$$\tau_\theta = -(J_z - J_x)\dot{\phi}\dot{\psi} + J_y\ddot{\theta}_d + J_y(\lambda_\theta + k_{1_\theta})\dot{e}_\theta + J_y\lambda_\theta k_{1_\theta} e_\theta + J_y k_{2_\theta} \mathrm{snl}(s_\theta) \tag{33}$$

$$\tau_\psi = -(J_x - J_y)\dot{\phi}\dot{\theta} + J_z\ddot{\psi}_d + J_z(\lambda_\psi + k_{1_\psi})\dot{e}_\psi + J_z\lambda_\psi k_{1_\psi} e_\psi + J_z k_{2_\psi} \mathrm{snl}(s_\psi) \tag{34}$$

Expressions (32), (33), and (34) represent the conceptual structure equivalent to that described in (16), (17) and (18). The function

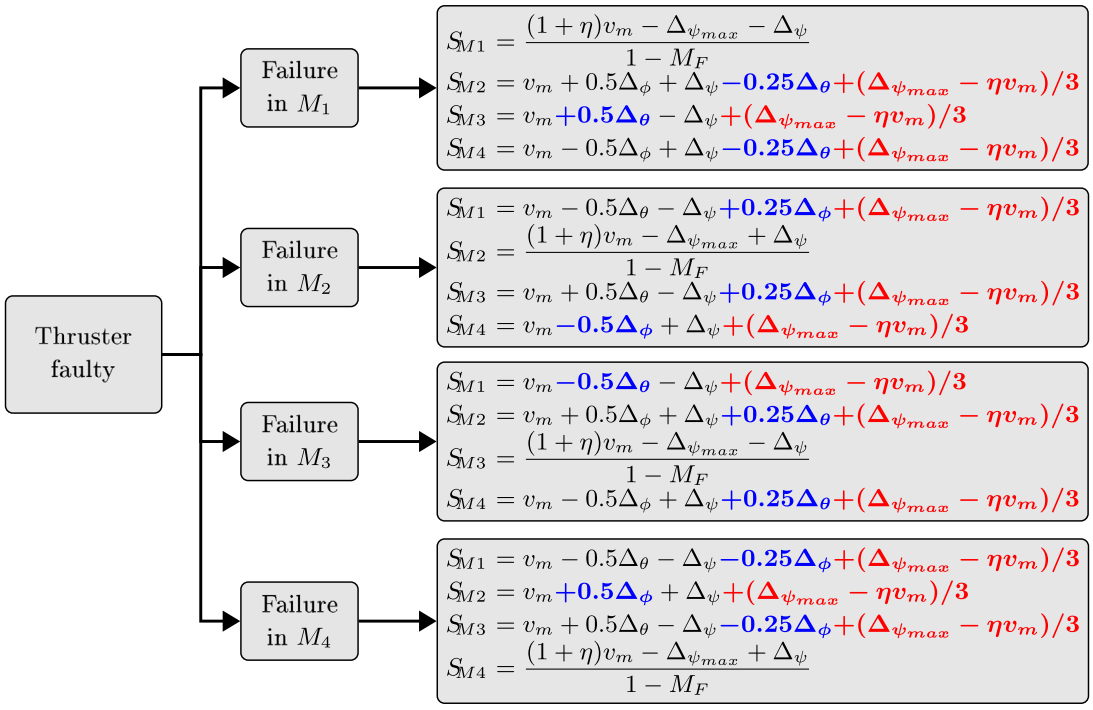

Fig. 5. Definition of S_{M1}, S_{M2}, S_{M3} and S_{M4} depending on the failed thruster. (For interpretation of the references to color in this figure legend, the reader is referred to the web version of this article.)

$\texttt{snl}(s_{(\cdot)})$ used in these expressions is analogous to the saturation function defined in (16), which serves the same purpose: to smooth the control action near the sliding surface and reduce the chattering phenomenon. Although different notations are used, both formulations are based on the same underlying principles. Therefore, these expressions can be interpreted as generalized and applied versions of the torque expressions presented in (16), (17), and (18). Based on these torque expressions, the control signal can then be adapted to act directly on the propellers.

The expression (7) relates the torques to the propeller speeds. To reduce the load on the faulty propeller, maintain the total thrust applied to all four motors, ensure altitude stability, and allow the methodology to be applied to commercial quadcopters, three rules are implemented in the auxiliary control system: (i) saturation of the faulty actuator, (ii) removal of tilt control from this actuator, and (iii) redistribution of the lift force among the other three actuators. The speed of the faulty actuator is limited in amplitude to prevent overloading, which could worsen the failure or extend the use of the defective equipment, ensuring that the quadcopter remains controllable.

In this approach, the controller sends a control signal to the propulsion system with a maximum amplitude of $a_{max} = \frac{(1+\eta)\cdot v_m}{1-M_F}$, ensuring that the actual thrust does not exceed η of the average thrust required to sustain the quadcopter, where η is the coefficient related to the percentage of the nominal power of the faulty propeller. To determine a_{max}, the auxiliary control system needs to know the amplitude of propeller failure, information obtained by comparing the current speed with the desired speed. With the saturated actuator, the control of the angle θ is removed if failure occurs in propellers M_1 or M_3, or the control of the angle ϕ is removed if failure occurs in propellers M_2 or M_4. The signal sent to the defective propeller S_{Mj} consists of the lifting force and the torque τ_ψ to assist in controlling the angle ψ, as given by (35), where $\Delta_{\psi_{max}}$ represents the maximum value that the variable Δ_ψ can assume, and the subscript j indicates the corresponding propeller.

$$S_{Mj} = \frac{(1+\eta)v_m - \Delta_{\psi_{max}} + (-1)^j \Delta_\psi}{1-M_F} \tag{35}$$

When the angle control of ϕ or θ is removed from the defective propeller, this function is fully transferred to the propeller on the opposite side. Fig. 5 illustrates the control signals sent to the propellers depending on which propeller experiences the failure. The lift force is redistributed among the other three propellers as follows: (i) the variation in force to control ϕ or θ is handled by the propeller opposite the faulty one, and (ii) the natural force variation of the faulty propeller is compensated. The variation in the lifting force for controlling ϕ or θ is equally distributed between the propellers adjacent to the defective one. In Fig. 5, the blue components represent the control of the angle ϕ or θ performed by the opposite propeller, as well as its redistribution to the adjacent propellers to balance the lift. The variation in the natural lifting force caused by the failure of the propeller is equally divided among the remaining propellers, as indicated by the red components.

3.6. Testing and validation of the proposed auxiliary control

The proposed algorithm is tested using a simulator based on the mathematical model of the quadcopter, allowing preliminary testing without the need for physical components such as bearings and batteries. This approach significantly reduces the time spent testing, analysis of results, and reconfiguration of controller parameters, speeding up the development of the auxiliary control system. The results obtained with the auxiliary control are compared with those observed when only the PID control system was in operation. To evaluate the performance of the auxiliary control system and minimize the impact of failure, the metric defined in (29) is used.

The parameter γ is defined as the desired value of the difference calculated by the metric (29) when comparing the simulation with the auxiliary control and the results of the platform with the PID control. If the results demonstrate a reduction greater than γ, particularly in the angles most affected by the failure, the auxiliary control system that uses SMC is experimentally validated on the test platform. Validation occurs when the experimental results in the region with active SMC control (RCA) closely match those obtained from the simulator, reducing errors in the analyzed angles and improving the quadcopter stabilization. The metrics given by (29) and (30) are used for this analysis.

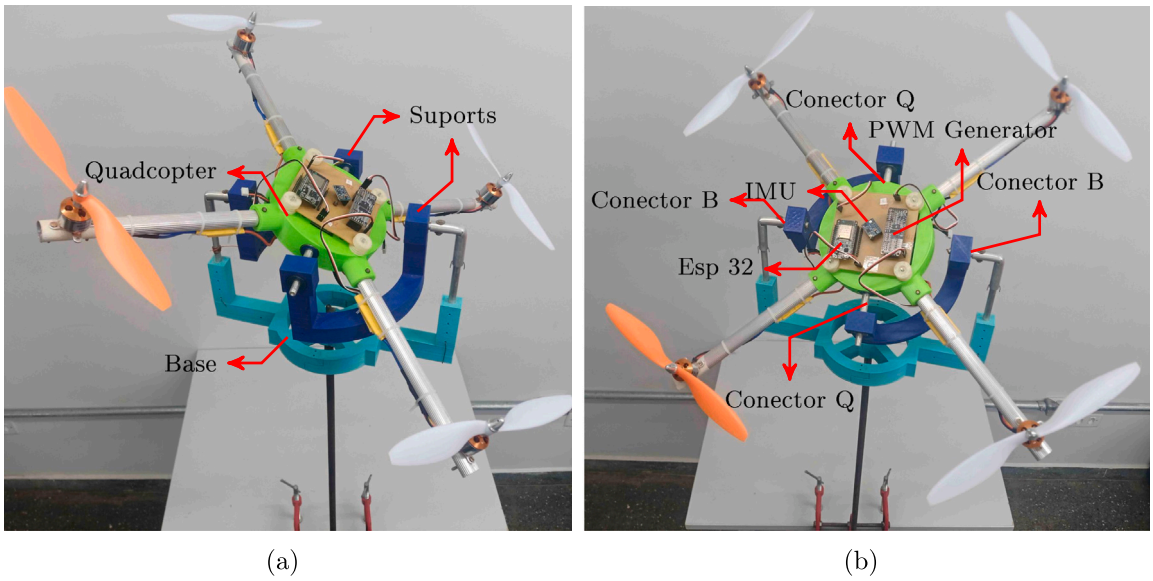

Fig. 6. Prototype of the testing platform: (a) relative to the supports and the base and (b) relative to the base only.

To ensure that the experimental validation is consistent with real operating conditions, the nonlinear simulator adopted in this study incorporates constraints that more accurately represent the physical behavior of the propulsion system. Sensor measurements account for noise and latency, and significant delays are modeled in the communication between the control system and the ESCs. Moreover, changes in propeller speed do not occur instantaneously after thrust redistribution commands; instead, they follow a gradual transition limited by both the ESC bandwidth and the motor dynamics. These features ensure that rapid thrust reallocations remain within the physical limits of the actuators, complying with real-world operational constraints.

4. Results

This section presents the results of applying the proposed methodology, including tests to analyze the dynamic behavior of the quadcopter during failures and the implementation of the auxiliary control system to respond to a reduction in power in any of the four propellers. The analysis includes comparisons between the simulated and experimental results, followed by a discussion of the findings. The development of the auxiliary control system was carried out in five stages, as detailed in the methodology and illustrated in Fig. 3.

4.1. Testing platform used for analyzing the quadcopter

This work uses the test platform developed and validated by Bulhes et al. [52] to simulate failure scenarios and analyze the behavior of the quadcopter, with the objective of developing a control system capable of mitigating the negative effects of power loss in one of the propellers. Fig. 6 presents the test platform used to observe the dynamic behavior of the quadcopter under these conditions. The platform allows the quadcopter to perform rotational movements while restricting translational movements. The roll and pitch angles are limited to the operational range of $\phi = \pm 25°$ and $\theta = \pm 25°$, while yaw movement has an unrestricted range of $\psi = \pm 180°$.

Fig. 6(a) presents the components of the test platform: (i) quadcopter, (ii) supports, and (iii) base. Fig. 6(b) presents the control board and connectors: (i) Connector B, which connects the base to the support via bearings, and (ii) Connector Q, which connects the support to the quadcopter through bearings, allowing for tilt movements. The flight controller used was the Esp 32, with inertial sensors from the GY-87 module, which includes accelerometers, gyroscopes, and magnetometers with measurement of the three axes. Communication between Esp 32 and the GY-87 Module occurs through the I2C protocol. The PWM signals were generated using the PCA9685 controller module, which receives commands from the Esp 32 via I2C and generates the necessary PWM signals for the four electronic speed controllers (ESC) [52].

4.2. Definition, analysis, and testing of failure scenarios on the test platform

For failure analysis, the propeller M_1, which rotates counterclockwise, was randomly selected. The experiments were divided into three temporal regions: (i) control system off, UR region, in yellow, (ii) control system on and operating without failure, CR region, in green, and (iii) control system on and operating with failure, FR region, in red. In the UR region, corresponding to the initial stage of each experiment, the control algorithm has not yet been executed and the errors at the angles ϕ, θ, and ψ are not corrected. Next, in the CR region, the PID control system is activated, stabilizing the quadcopter and eliminating errors at the aforementioned angles. The FR region begins approximately $t_F = 9$ s after the transition from UR, at which point the failure is introduced, reducing the propeller power M_1. This time interval is sufficient to stabilize the quadcopter before the failure is applied.

For standardization, $\phi_d = 0$, $\theta_d = 0$, and $\psi_d = 0$ were used. Furthermore, all experiments were initialized with $\phi_i \approx 20°$, $\theta_i \approx 20°$, and $\psi_i \approx 90°$. The last angle, ψ_i, was more variable between experiments due to the manual nature of holding the quadcopter in the desired position before reaching the CR region, at which point the quadcopter was released to avoid the influence of external forces during the transient phase. Preliminary tests indicated that the system maintained stable control up to $M_F = 24\%$, a value assigned to the parameter $M_{F_{max}}$. Therefore, the experiments were conducted with $0 \leq M_F \leq M_{F_{max}} = 24\%$, in increments of 2%, resulting in a total of thirteen experiments with equally distributed values of M_F.

4.2.1. Data collection and analysis during failures

Fig. 7 presents the results obtained from the experiment in which the failure was set to $M_F = 0\%$, using the test platform. This scenario represents the situation where no failure occurs throughout the experiment and serves as a reference for the expected dynamics of the system without failures. In Fig. 7(a), the measurements of ϕ, θ and ψ are shown in brown, green, and purple, respectively. In the figure, the dashed red

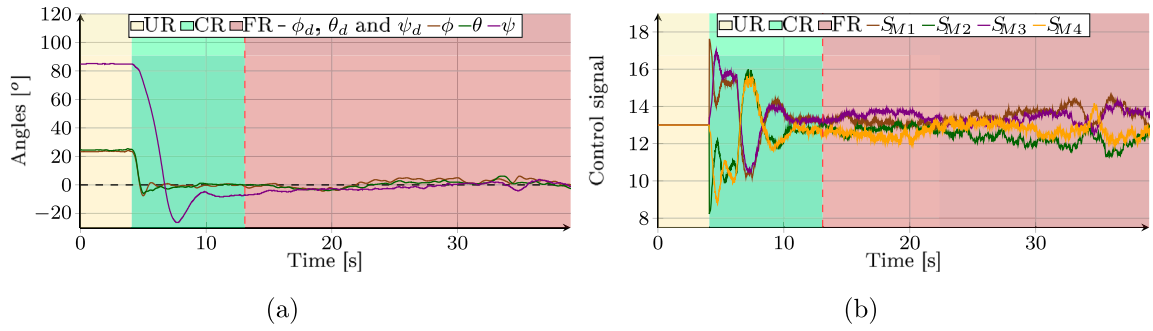

Fig. 7. Failure analysis with $M_F = 0\%$: (a) ϕ, θ and ψ, and (b) control signal sent to PCA. (For interpretation of the references to color in this figure legend, the reader is referred to the web version of this article.)

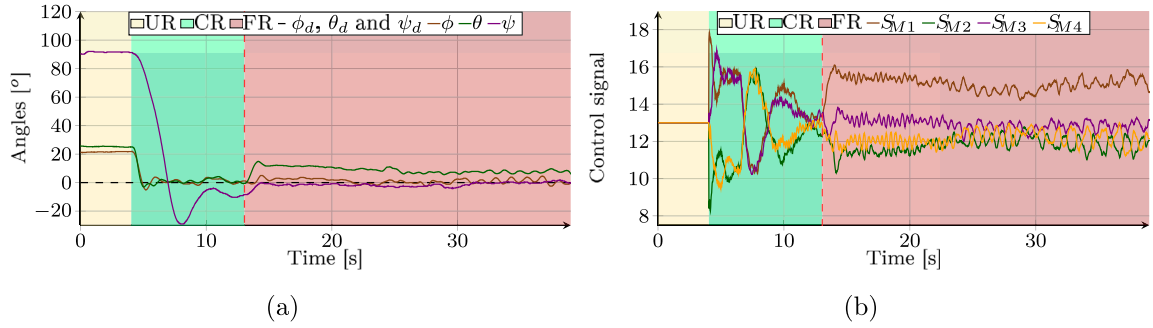

Fig. 8. Failure analysis with $M_F = 14\%$: (a) ϕ, θ and ψ, and (b) control signal sent to PCA.

vertical line indicates the moment when the failure occurs, in the FR region. Once the control system is activated, the angles oscillate around 0°, keeping the error close to zero. The system stabilizes in less than 5 s, and only minor variations are observed thereafter.

Fig. 7(b) presents the four signals sent to the PCA controller for propeller control. Initially, there is a noticeable difference between signals S_{M1} and S_{M3} compared to signals S_{M2} and S_{M4}, due to control efforts to reduce angle error ψ. After the system reaches steady state, all four signals oscillate around a central value that controls the operating altitude of the quadcopter, defined as $v_m = 13$ in this study, with variations of approximately ±2 around the mean. Fig. 8 presents the results of the experiment with a failure of $M_F = 14\%$. Fig. 8(a) illustrates the behavior of ϕ, θ, and ψ, demonstrating the change caused by the failure of the angle θ, which deviates from the reference value θ_d, reaching values above 10°. The variations in ϕ and ψ were not significant in this experiment.

Fig. 8(b) presents the behavior of the four signals sent to the PCA controller for the propellers. After failure, the signal S_{M1} diverges from the others, indicating that the control system, unable to resolve the issue, requests more power from the faulty propeller. This, in turn, affects the signal S_{M3}, which works in conjunction with S_{M1} to control the angle θ. Fig. 9 presents the results of the experiment with a failure of $M_F = 24\%$. Fig. 9(a) presents the dynamic behavior of the angles analyzed, where, after failure, the angle θ changes slowly, slowly decreasing from 20° over time. Furthermore, the angle ψ oscillates outside the reference but stabilizes around $t \approx 35$ s, which may be related to the reduction in the angle error θ.

Fig. 9(b) displays the dynamic behavior of the four signals sent to the PCA controller for the propellers. In this experiment, especially in the moments immediately after failure, the signal S_{M1} operated with an amplitude above 16, reaching oscillations close to 18. This reflects the controller's attempt to increase the force on this motor to correct the θ angle. Furthermore, the signals S_{M2} and S_{M4} exhibited a similar dynamic behavior, indicating that the failure had little influence on the angle control ϕ, as observed in Fig. 9(a). This experiment showed the greatest power loss among all the tests, as for $M_F = 26\%$, the system completely lost control of ψ and θ, reaching the limits imposed by the test platform for these angles, which complicated the interpretation of the results. The average values observed in all experiments after the onset of the failure are presented in Fig. 10.

Fig. 10(a) shows the average variation of the angles analyzed in all experiments. The curves representing the error in ϕ and θ exhibit uniform variations in most experiments, with the exception of the error curve ψ, which presents an outlier deviation in the experiment with $M_F = 24\%$. The error in ϕ remains nearly constant as the failure in the propeller M_1 increases, similar to the behavior of the error ψ in $M_F \leq 22\%$. In contrast, the error in θ increases almost linearly as the failure intensifies in the experiments.

Fig. 10(b) displays the average values observed for signals S_{M1}, S_{M2}, S_{M3} and S_{M4}. Signals S_{M2} and S_{M4} decrease as M_F increases, in an attempt to compensate for the torque τ_ψ and maintain control of the angle ψ. Furthermore, as shown in Figs. 8(b) and 9(b), signal S_{M1} increases as the controller tries to adjust the angle θ, which could overload the damaged propeller, as the control system demands more thrust from this propeller. The signal S_{M3}, on the other hand, remains almost constant throughout the experiments. After analyzing the quadcopter's behavior in each experiment, the mathematical model was evaluated to verify if it adequately represents the rotational dynamics of the quadcopter with a failure in one of the actuators.

4.2.2. Comparison between experiment and simulation

The $D_{MQ_{(\phi)(\theta)(\psi)}}$ values obtained from the practical and simulated experiments are presented in Table 3. The blue values indicate the scenario with the smallest difference between the practical and simulated data, while the red values indicate the scenario with the largest observed difference in the comparison of these parameters.

For angle ϕ, the values D_{MQ_ϕ} remained close to 2° in almost all failure scenarios, both in the simulator and in practice. The smallest difference between the simulated and practical D_{MQ_ϕ} values occurred with a 8% failure, while the largest difference was observed with a 24% failure. In the case of the angle θ, which was most affected by the failure in M_1 during practical experiments, the values D_{MQ_θ}

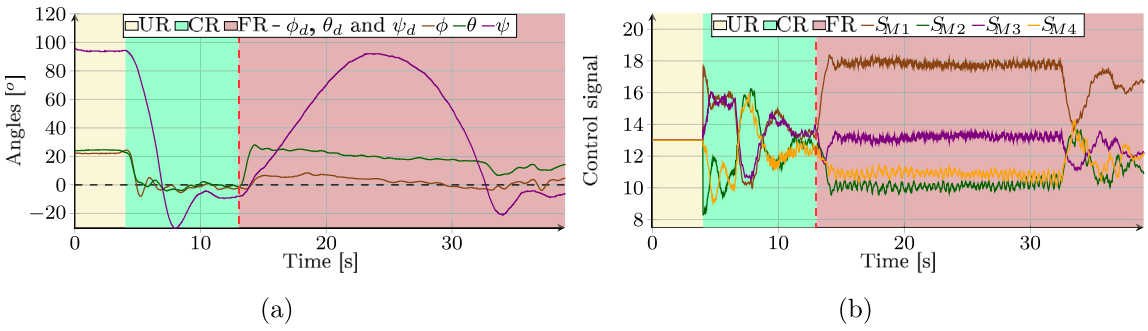

Fig. 9. Failure analysis with $M_F = 24\%$: (a) ϕ, θ and ψ, and (b) control signal sent to PCA.

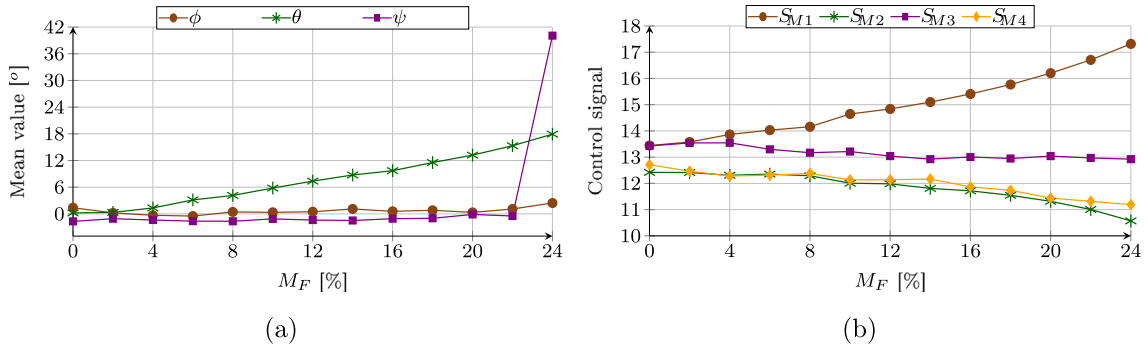

Fig. 10. Comparative analysis for all values of M_F tested: (a) the mean of the angles and (b) the mean control signal sent to the PCA.

Table 3
Comparison between the $D_{MQ_{(\phi)(\theta)(\psi)}}$ obtained in practical experiments and in simulations using PID control.

Angle	Type	M_F [%]											
		2	4	6	8	10	12	14	16	18	20	22	24
ϕ	Plat [°]	2.1	1.3	1.9	**2.1**	1.3	1.3	1.9	1.2	1.8	1.8	2.3	**4.0**
	Sim [°]	2.0	2.0	2.0	**2.1**	1.9	1.9	1.9	2.0	1.8	2.0	2.0	**2.1**
	E_{q_ϕ} [%]	0.6	2.6	0.2	0.0	2.1	1.9	0.2	2.8	0.2	0.8	0.9	7.1
θ	Plat [°]	2.4	2.0	3.7	4.3	5.7	7.4	8.8	**9.6**	11.7	13.4	15.8	**18.4**
	Sim [°]	1.1	1.4	2.5	3.7	4.9	6.3	7.8	**9.4**	11.0	12.6	14.5	**16.1**
	E_{q_θ} [%]	4.9	2.3	4.2	2.0	2.4	3.4	3.0	0.6	1.8	2.2	3.3	5.5
ψ	Plat [°]	1.8	1.7	2.5	2.0	**1.1**	1.7	1.8	1.2	1.3	0.9	3.0	**59.2**
	Sim [°]	2.1	1.8	1.6	1.3	**1.2**	0.9	0.7	0.6	0.6	0.7	2.3	**47.2**
	E_{q_ψ} [%]	0.1	0.0	0.5	0.3	0.0	0.4	0.6	0.3	0.3	0.1	0.4	5.2

showed a gradual increase in both practical and simulated experiments as the failure intensified. The largest difference between the simulated and practical D_{MQ_θ} values was observed with a 24% failure, with a difference of approximately 2.3°, while the smallest difference occurred with a failure 16%, differing by 0.2°.

For angle ψ, the values D_{MQ_ψ} ranged between 0.6° and 2.5° in most of the scenarios analyzed. The smallest difference between the simulated and practical D_{MQ_ψ} values was observed with $M_F = 10\%$, while the largest difference occurred with $M_F = 24\%$, resulting in approximately 12.0°. The values of $E_{Q_{(\phi),(\theta),(\psi)}}$ remained close to zero, except in the scenario with $M_F = 24\%$, where E_{Q_ϕ}, E_{Q_θ} and E_{Q_ψ} were 7.1%, 5.5%, and 5.2%, respectively. The global mean square percentage error $E_{q_{global}}$, calculated as the average of E_{Q_ϕ}, E_{Q_θ}, and E_{Q_ψ}, was 1.76%.

Fig. 11 presents the comparison of the results obtained for the quadcopter prototype using the test platform and the proposed nonlinear mathematical model, both subjected to a failure of $M_F = 12\%$. Fig. 11(a) shows the comparison of the S_{M1} signal sent to the PCA controller, where the brown curve represents the experimental result, and the black curve represents the simulator result. Both curves exhibit similar behavior throughout the analyzed interval. Fig. 11(b) presents the comparison of the S_{M2} signal sent to the PCA controller, with the green curve representing the experimental result and the black curve representing the simulator result. In both analyses, the dynamic behavior observed in the experiment was successfully replicated by the nonlinear simulator.

Fig. 11(c) shows the comparison of the S_{M3} signal sent to the PCA controller, with the purple curve representing the experimental result and the black curve representing the simulator result. Similarly, Fig. 11(d) presents the comparison of the signal S_{M4}, where the yellow curve represents the experimental result and the black curve represents the simulator result. These results indicate that in the studies conducted, the control signals S_{M1}, S_{M2}, S_{M3}, and S_{M4} generated by the nonlinear simulator successfully describe the behavior of the real signals sent by the onboard quadcopter controller to the PCA controller in the failure scenario with $M_F = 12\%$. Fig. 11(e) presents the behavior of the angle ϕ for practical and simulated experiments. It is observed that, both at the start of the control system and after failure initiation, the curves representing the angle ϕ – experimental (in brown) and simulated (in black) – exhibit similar behaviors.

Fig. 11(f) displays the behavior of the angle θ in both practical and simulated experiments. The green curve represents the angle θ in the experiment, while the black curve represents the simulated angle θ. Both curves exhibit similar signal patterns, particularly during

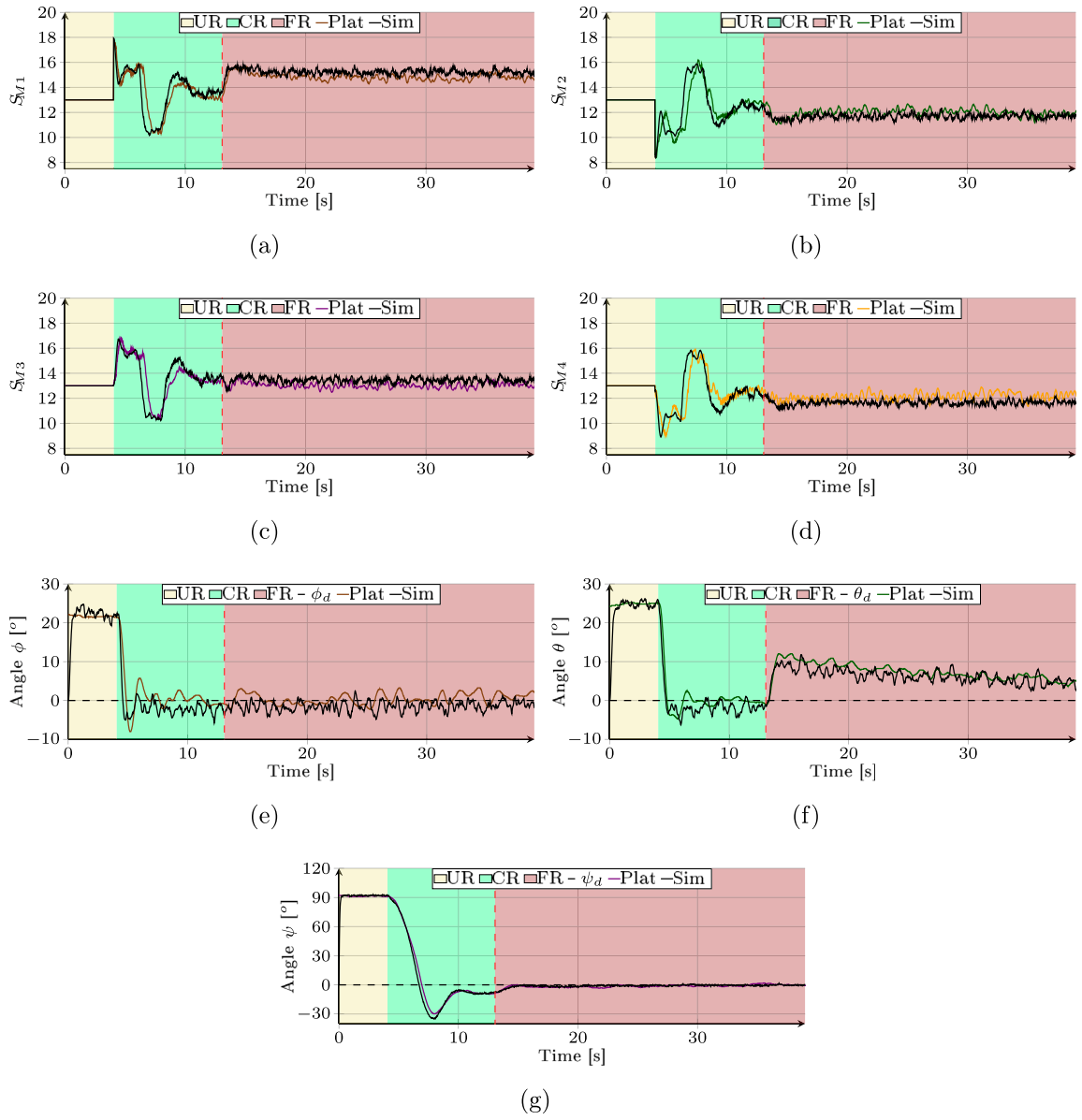

Fig. 11. Comparison between simulated experiment and using the test platform with $M_F = 12\%$: (a) S_{M1}, (b) S_{M2}, (c) S_{M3}, (d) S_{M4}, (e) ϕ, (f) θ and (g) ψ. (For interpretation of the references to color in this figure legend, the reader is referred to the web version of this article.)

transitions when the PID control system is activated and when failure begins. Furthermore, both signals exhibit a tendency for the θ angle to decrease over time in the failure region.

The comparison between the experimental and simulated angle signals ψ is presented in Fig. 11(g). The purple curve represents the experimental angle ψ, while the black curve represents the simulated angle ψ. It is observed that the transients of both curves exhibit similar behavior and that the failure does not significantly alter the values of this angle between the experimental and simulated curves. Fig. 12 shows the comparison between the results obtained for the quadcopter prototype on the test platform and with the nonlinear simulator, both subjected to failure of $M_F = 22\%$. Fig. 12(a) presents the comparison of the S_{M1} signal sent to the PCA controller. The brown curve represents the experimental result, while the black curve represents the simulation result. The brown and black curves are similar throughout most of the analyzed interval, both in the control region and the failure region, with small differences observed at certain moments, such as after $t > 30$ s.

Fig. 12(b) presents the comparison of the S_{M2} signal sent to the PCA controller. The green curve represents the experimental result, while the black curve shows the simulation result. Similarly to Fig. 12(a), the green and black signals exhibit a similar behavior over time, with small differences observed at specific intervals, such as after $t > 30$ s. Fig. 12(c) compares the S_{M3} signal sent to the PCA controller. The purple curve represents the experimental result, while the black curve represents the simulation result. Both signals exhibit similar dynamics, with no significant divergences between the curves in the analyzed interval. Finally, Fig. 12(d) compares the S_{M4} signal sent to the PCA controller, with the yellow curve representing the experimental result and the black curve representing the simulator result.

Fig. 12(e) illustrates the behavior of the angle ϕ for the practical experiment and the simulation using the nonlinear model. As observed in Fig. 11(e), the simulated angle ϕ corresponds closely to the angle ϕ obtained experimentally, with no visible differences between the signals after the onset of the failure, indicating that the failure does not significantly influence the control of the angle ϕ. Fig. 12(f) displays the behavior of the angle θ for the practical experiment and the simulation. The green curve represents the experimental angle θ, while the black curve corresponds to the simulated angle θ. At the onset of failure, both

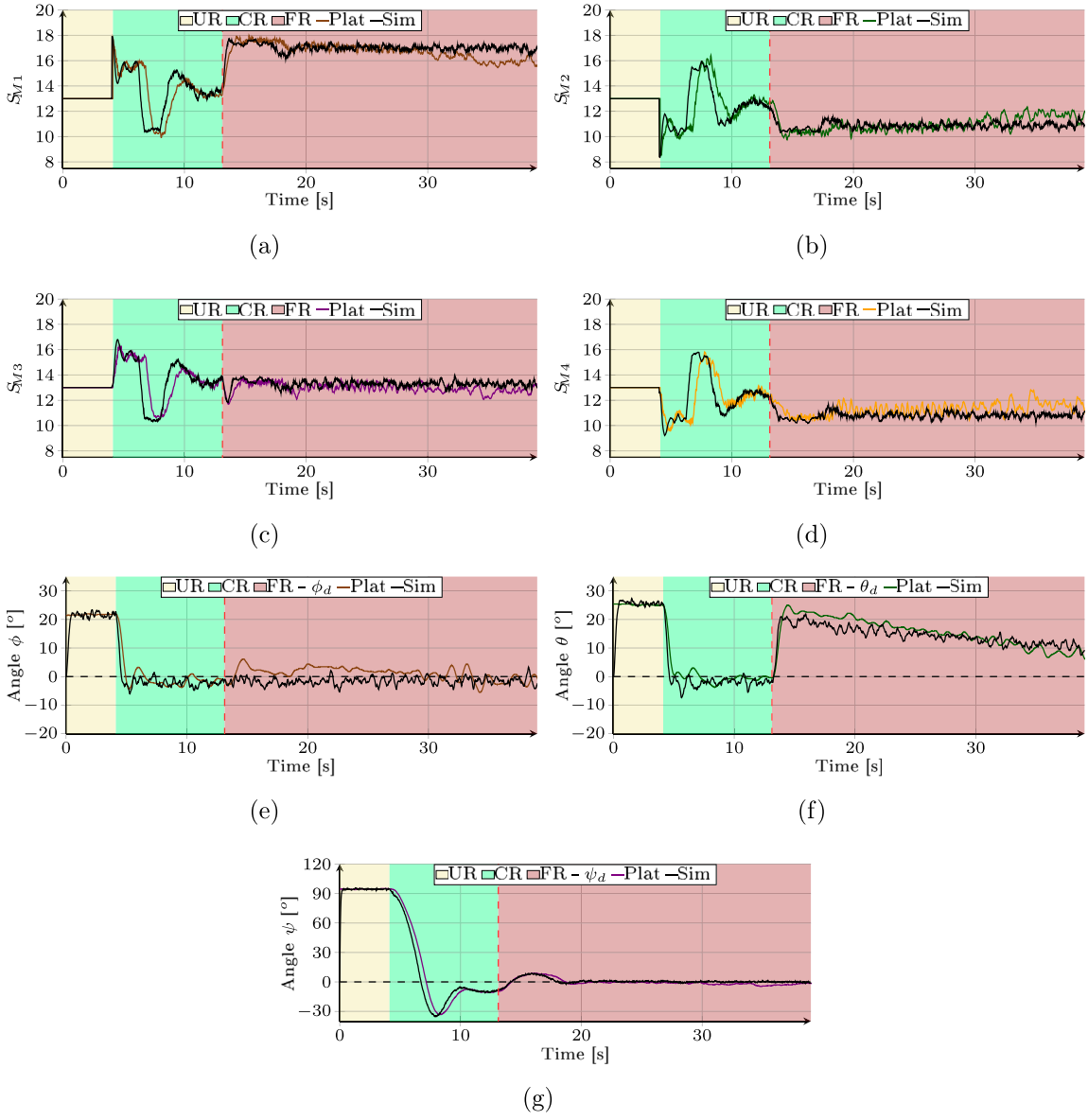

Fig. 12. Comparison between simulated experiment and using the test platform with $M_F = 22\%$: (a) S_{M1}, (b) S_{M2}, (c) S_{M3}, (d) S_{M4}, (e) ϕ, (f) θ and (g) ψ. (For interpretation of the references to color in this figure legend, the reader is referred to the web version of this article.)

signals exhibit significant changes; over time, the amplitude of θ in both the simulated and experimental signals gradually decreases.

The comparison between the experimental and simulated ψ signals is presented in Fig. 12(g). The purple curve represents the experimental angle ψ, while the black curve represents the simulated angle ψ. Upon the occurrence of the failure, the purple curve deviates from its desired value, reaching a maximum amplitude of approximately 10.0° before returning after approximately 7 s, a behavior also observed in the simulated curve. As shown in Figs. 11 and 12, the simulator produces responses similar to those observed in practical experiments carried out on the test platform. The global mean square percentage error $E_{q_{global}}$, calculated for the 12 experiments listed in Table 3, is 1.76%. Given that $\kappa_q = 2\%$ is the acceptable error threshold, it can be concluded that the nonlinear simulator adequately represents the test platform in propeller failure scenarios. Therefore, the simulator can be used for the development of the SMC auxiliary control system, which operates during failures to mitigate adverse effects.

4.3. System and operation of sliding mode auxiliary control

The parameter Δ_d is set to 2 s, ensuring that the flight controller has enough time to detect the failure in real situations and allow its effects to be observed at controlled angles. During this interval, the controller identifies that the commands sent to the system are not producing the expected results, indicating a failure in one of the propellers. The control algorithm is then switched from PID to SMC, in order to mitigate the effects of actuator failure M_1, focusing mainly on the angle θ. After 2 s from the appearance of the failure, the PID control is replaced by the SMC control, entering the region with active SMC control, known as ACR.

Modern fault detection systems are capable of identifying anomalies in less than 0.7 s, as demonstrated in recent studies [53–55]. Therefore, the detection time $\Delta_d = 2$ s adopted in this study is conservative and can be reduced in practical applications, which may improve the performance of the proposed auxiliary control system. The earlier a fault is detected, the smaller the attitude deviations at the time of corrective action, making stabilization more effective. It is important to note that the objective of this work is not to diagnose the fault but

Table 4
Parameters obtained for the proposed SMC controller.

Angle	Lyapunov			Adopted parameters		
	λ	k_1	k_2	λ	k_1	k_2
ϕ	$\lambda_\phi > 0$	$k_{1_\phi} > 0$	$k_{2_\phi} > 0$	5	5	0.3
θ	$\lambda_\theta > 0$	$k_{1_\theta} > 0$	$k_{2_\theta} > 0$	10	6	0.3
ψ	$\lambda_\psi > 0$	$k_{1_\psi} > 0$	$k_{2_\psi} > 0$	5	5	0.3

to ensure an effective response once a fault is present. To this end, additional constraints were incorporated into the controller to reduce the effects of propeller failure M_1.

Additional constraints were imposed on the controller: (i) limiting the maximum power requested from the propeller M_1 and (ii) increasing the control efforts in M_2 and M_4 to compensate for the thrust loss caused by failure. The goal of limiting the power requested from the faulty propeller is to prevent the failure from worsening, further compromising the device's controllability. Thus, $\eta = 0.1$ is defined so that the maximum value requested from the faulty propeller does not exceed 10% of υ_m. The increased control efforts in M_2 and M_4 help balance the total thrust of the system, maintaining controlled altitude during flight. During practical experiments, although the failure in M_1 reduced the total thrust, the lift of the quadcopter was not affected because the tests were conducted on the test platform, ensuring the stability of the device without variation in altitude.

With the SMC control implemented, tests were conducted on the nonlinear mathematical model to evaluate the behavior of the angles ϕ, θ and ψ during the failure of one of the actuators. These tests allowed for the adjustment of the parameters presented in Table 4, with the goal of ensuring a satisfactory response under adverse conditions. Once all parameters were defined, the SMC control was implemented.[2] Table 4 presents the parameter limits for λ, k_1, and k_2 for each angle, which meets the Lyapunov stability criterion. It is noted that due to the more significant impact of the failure on the angle θ, the parameter λ_θ was set to a value twice that of λ_ϕ and λ_ψ. The value of k_2 for the controllers ϕ, θ and ψ was kept close to zero to minimize the undesirable effects of switching caused by the sign function.

The auxiliary control system parameters, k_1, k_2, and λ, were empirically determined based on simulations using the nonlinear simulator, while ensuring compliance with the Lyapunov stability criteria. This approach allowed the system's convergence to be assessed under different fault scenarios. However, the performance of the system could be further improved by applying optimization techniques to automatically adjust these parameters within the same simulation environment, ensuring stability and efficiency under operational constraints. Once the parameters were defined, quantitative comparisons were made between the performance of the PID and SMC controllers at varying fault levels.

Table 5 presents the results $D_{MQ_{(\phi)(\theta)(\psi)}}$ obtained from the simulator using PID and SMC controls. The blue values indicate the smallest difference obtained between $D_{MQ_{(\phi)(\theta)(\psi)}}$ in the PID and SMC simulations, while the red values indicate the largest difference. In the platform experiment, the maximum value $M_{F_{max}}$ was 24% with PID control. In the simulator, failures of up to $M_F = 30\%$ were possible for both controllers. For the angle ϕ, the value D_{MQ_ϕ} generated by the SMC control was slightly higher than that obtained with the PID control, the largest difference recorded at $M_F = 30\%$, which was 1.4°.

For the angle θ, which is most affected by propeller failure M_1, the value D_{MQ_θ} increases almost linearly in the simulator with PID control, while with SMC control, the value D_{MQ_θ} remains nearly stable at approximately 4.3°. In scenarios of minor failures, this parameter alone may not justify the use of SMC control. However, SMC control improves the performance of the system when $M_F \geq 10\%$, becoming more efficient as the failure intensifies. On the platform, for the angle ψ, where the values of D_{MQ_ψ} with the PID control start to diverge for $M_F \geq 24\%$, the SMC control allows control up to $M_F = 30\%$. Furthermore, SMC control improves D_{MQ_ψ} in most of the scenarios analyzed, except between $16\% \leq M_F \leq 20\%$, where PID control outperforms SMC control for angle ψ.

Fig. 13 presents the results obtained using the SMC control strategy for $M_F = 10\%$. In the figure, the dashed red vertical line marks the moment of failure in the FR region, whereas the dashed blue line indicates the activation of the auxiliary control in the ACR region. Fig. 13(a) shows the S_{M1} signal sent to the PCA controller to activate the propeller M_1. The brown curve represents the practical behavior observed with the PID control, while the turquoise curve represents the value obtained with the SMC control. It is observed that in the ACR region, where the SMC control is active, the S_{M1} signal remains saturated at $a_{max} \approx 16$ for an extended period. This prevents the ESC of the faulty motor from receiving a control signal $S_{M1} > a_{max}$, which, for $M_F = 10\%$, results in a force equivalent to 14.3, corresponding to $1 - M_F$ of a_{max} or $1 + \eta$ of the average thrust υ_m, with $\eta = 0.1$ and $\upsilon_m = 13$.

Figs. 13(b), 13(c), and 13(d) present the responses to S_{M2}, S_{M3}, and S_{M4}, respectively. The green curve represents the S_{M2} signal, the purple curve represents the S_{M3} signal, and the yellow curve represents the S_{M4} signal, all collected on the test platform using the PID controller. The turquoise curves correspond to the signals sent to the PCA controller to control the fault-free propellers. It is observed that in the ACR region, the turquoise curves exhibit greater oscillation compared to the signals collected with the PID control. This behavior can be attributed to the switch induced by the sign function $\mathtt{snl}(x)$.

Fig. 13(e) presents the behavior of the angle ϕ. The brown curve indicates the behavior of this parameter with the PID controller, while the turquoise curve represents the simulated behavior using the SMC control, initiated 2 s after the onset of the failure. The results of the nonlinear simulator showed similar characteristics between the performance of the PID control and the SMC control. Fig. 13(f) presents the behavior of the angle θ. The green curve represents the data collected on the test platform with PID control, while the turquoise curve represents the angle response θ obtained with the SMC control. It is observed that the error in the variable θ was mitigated by the efforts of the SMC controller.

The response of the variable ψ for the control of the SMC is presented in Fig. 13(g). The purple curve represents the experimental angle ψ with the PID control, while the turquoise curve represents the SMC control after the failure was diagnosed. No significant changes were observed in this variable when using the SMC control. Fig. 14 presents the results for the SMC control with $M_F = 24\%$. Fig. 14(a) shows the S_{M1} signal sent to the PCA controller for the propeller M_1, with the brown curve representing the practical behavior under PID control and the turquoise curve representing the SMC control. It is observed that in the ACR region, where the SMC control is active, the S_{M1} signal remains saturated at $a_{max} \approx 19$ for some moments. This prevents the faulty motor from receiving a control signal $S_{M1} > a_{max}$, which, for $M_F = 24\%$, corresponds to a control force equivalent to 14.3, representing $1 - M_F$ of a_{max} or $1 + \eta$ of the average thrust υ_m, with $\eta = 0.1$ and $\upsilon_m = 13$.

Figs. 14(b), 14(c), and 14(d) present the responses of S_{M2}, S_{M3}, and S_{M4}, respectively. The turquoise curve represents the signals sent to the PCA controller for the fault-free propellers, while the other curves represent the signals collected from the quadcopter prototype. In addition to the oscillations in the SMC control signals, caused by the switching phenomenon, there is also a noticeable difference in the behavior of the practical curves between the beginning and the end of the experiment. This can be attributed to the nature of the control applied in each region. Fig. 14(e) illustrates the behavior of the angle ϕ. The brown curve represents this parameter using the PID controller,

[2] The routines containing the nonlinear simulator integrated with the SMC control are available on the Code Ocean computational reproducibility platform [56].

Table 5
Comparison between the $D_{MQ_{(\phi)(\theta)(\psi)}}$ obtained in the simulations using the PID control and the SMC control with $\eta = 10\%$.

Angle	Type	M_F														
		2	4	6	8	10	12	14	16	18	20	22	24	26	28	30
ϕ	PID	2.0	2.0	2.0	2.1	1.9	1.9	1.9	2.0	1.8	2.0	2.0	2.1	1.4	**2.4**	**4.0**
	SMC	2.6	2.5	2.6	2.7	2.5	2.7	2.6	2.6	2.6	2.6	2.6	2.5	2.5	**2.6**	**2.6**
θ	PID	1.1	1.4	2.5	3.7	**4.9**	6.3	7.8	9.4	11.0	12.6	14.5	16.1	18.2	19.0	**19.7**
	SMC	4.4	4.3	4.3	4.4	**4.3**	4.3	4.2	4.3	4.3	4.2	4.2	4.1	4.2	4.1	**4.1**
ψ	PID	2.1	1.8	1.6	1.3	1.2	0.9	**0.7**	0.6	0.6	0.7	2.3	47.2	315.0	503.5	**742.2**
	SMC	0.9	0.9	0.5	0.5	0.5	0.6	**0.6**	0.7	0.8	0.8	1.3	3.0	8.3	16.8	**19.3**

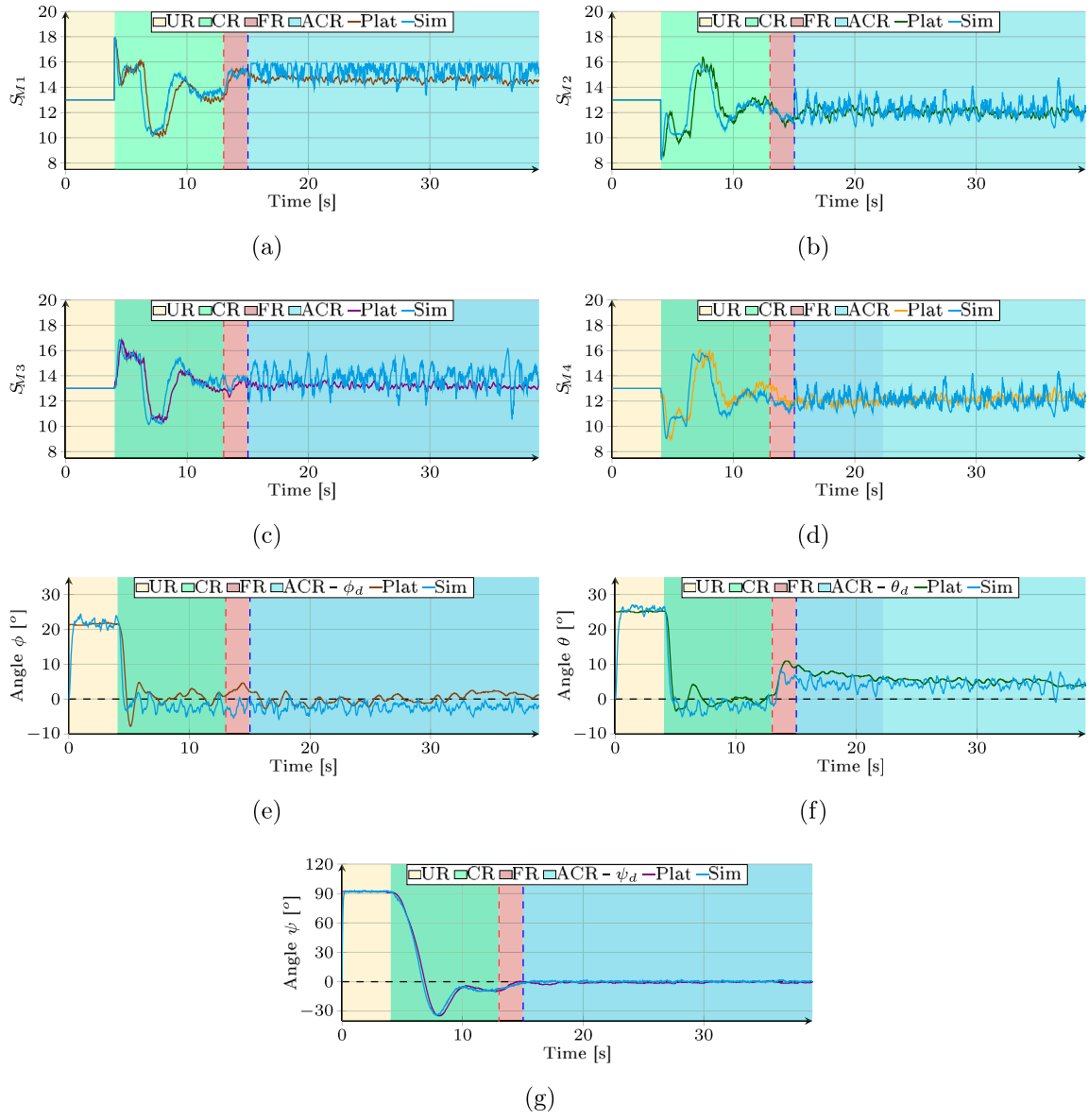

Fig. 13. Comparison between practical experiment with PID control and simulated with SMC control for $M_F = 10\%$: (a) S_{M1}, (b) S_{M2}, (c) S_{M3}, (d) S_{M4}, (e) ϕ, (f) θ and (g) ψ. (For interpretation of the references to color in this figure legend, the reader is referred to the web version of this article.)

while the turquoise curve represents the behavior with the SMC control 2 s after the failure onset. Similarly to the results in Fig. 13(e), the angle ϕ was not significantly affected by the introduction of the SMC control.

Fig. 14(f) shows the behavior of the angle θ. The green curve presents the data collected on the test platform with PID control, while the turquoise curve represents the angle response θ with SMC control. Angle error θ was reduced by the efforts of the SMC controller, similar to the observation in Fig. 13(f). The value of D_{MQ_θ} obtained on the platform was 18.4°, while in the simulation with SMC control, D_{MQ_ψ} was 4.1°, maintaining control of ψ for this failure magnitude.

The curves illustrating the behavior of the variable ψ are presented in Fig. 14(g). For a failure with $M_F = 24\%$, the SMC control demonstrated significant results, effectively mitigating the divergent behavior of ψ after the failure. In the CR region, the turquoise curve corresponds to the PID control and when the failure is introduced, the variable ψ deviates from the desired value. The SMC control corrects

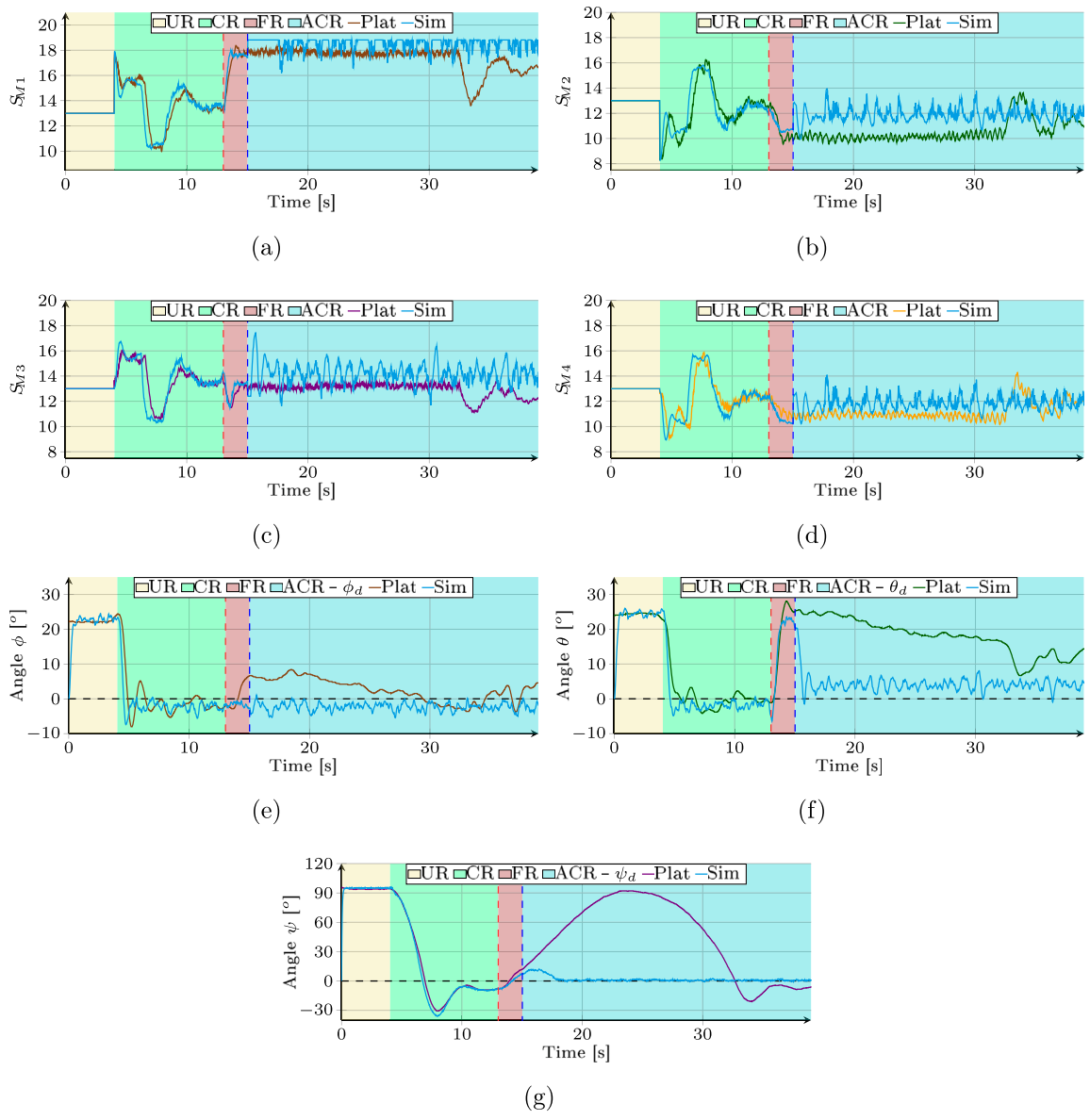

Fig. 14. Comparison between practical experiment with PID control and simulated with SMC control for $M_F = 24\%$: (a) S_{M1}, (b) S_{M2}, (c) S_{M3}, (d) S_{M4}, (e) ϕ, (f) θ and (g) ψ. (For interpretation of the references to color in this figure legend, the reader is referred to the web version of this article.)

for this divergence before the signal becomes unstable. The value D_{MQ_ψ} obtained on the test platform was 59.2°, while the simulated value with SMC control was 3.0°, maintaining control of ψ at this magnitude of failure. Furthermore, the observed deviation in ψ occurred before the auxiliary control system became active, two seconds after the failure in M_1, and this deviation was mitigated as soon as the controller regained authority over θ, which was the most affected by the failure in M_1. To support these findings and assess the consistency of the results, a statistical analysis was performed using the t-student distribution with a confidence level 95%.

To further assess the performance of the proposed control strategy, 25 simulations were conducted for three different failure levels: $M_F = 8\%$, 16%, and 24%. To verify the suitability of using the t-student test for the estimation of the confidence interval, the Kolmogorov–Smirnov test was applied to evaluate the adherence of the data to a normal distribution. The results confirmed the null hypothesis of normality, validating the statistical approach adopted. Fig. 15 presents the analysis of the empirical cumulative distribution functions for $M_F = 24\%$, comparing the PID controller and the proposed auxiliary controller for the variables D_{MQ_ϕ}, D_{MQ_θ}, and D_{MQ_ψ}. The blue curves represent the empirical cumulative distributions obtained from the simulations, while the red curves correspond to the standard normal cumulative distribution function. The close alignment between these curves reinforces the statistical consistency of the results and supports the use of the inferential methods employed.

The confidence intervals for $D_{MQ_{(\phi)(\theta)(\psi)}}$ were obtained from 25 simulations for three different failure levels $M_F = 8\%$, 16% and 24%. Table 6 presents the sample means μ, standard deviations σ, and confidence intervals C_i for each controller and each attitude angle. The standard deviations were low in most cases, except for ψ under $M_F = 24\%$, which showed a higher dispersion and thus a wider confidence interval [32.85° to 42.73°].

Comparing the performance of the proposed auxiliary controller and the PID controller, it is observed that for angle ϕ, the mean values and standard deviations were similar in all three failure levels tested. For θ, the auxiliary controller produced mean values approximately twice as low as those of the PID for $M_F = 16\%$, and nearly four times lower for $M_F = 24\%$, while maintaining slightly lower standard deviations. Finally, for ψ, both controllers performed similarly in $M_F = 8\%$ and 16%, but in $M_F = 24\%$, the mean of the auxiliary controller was about

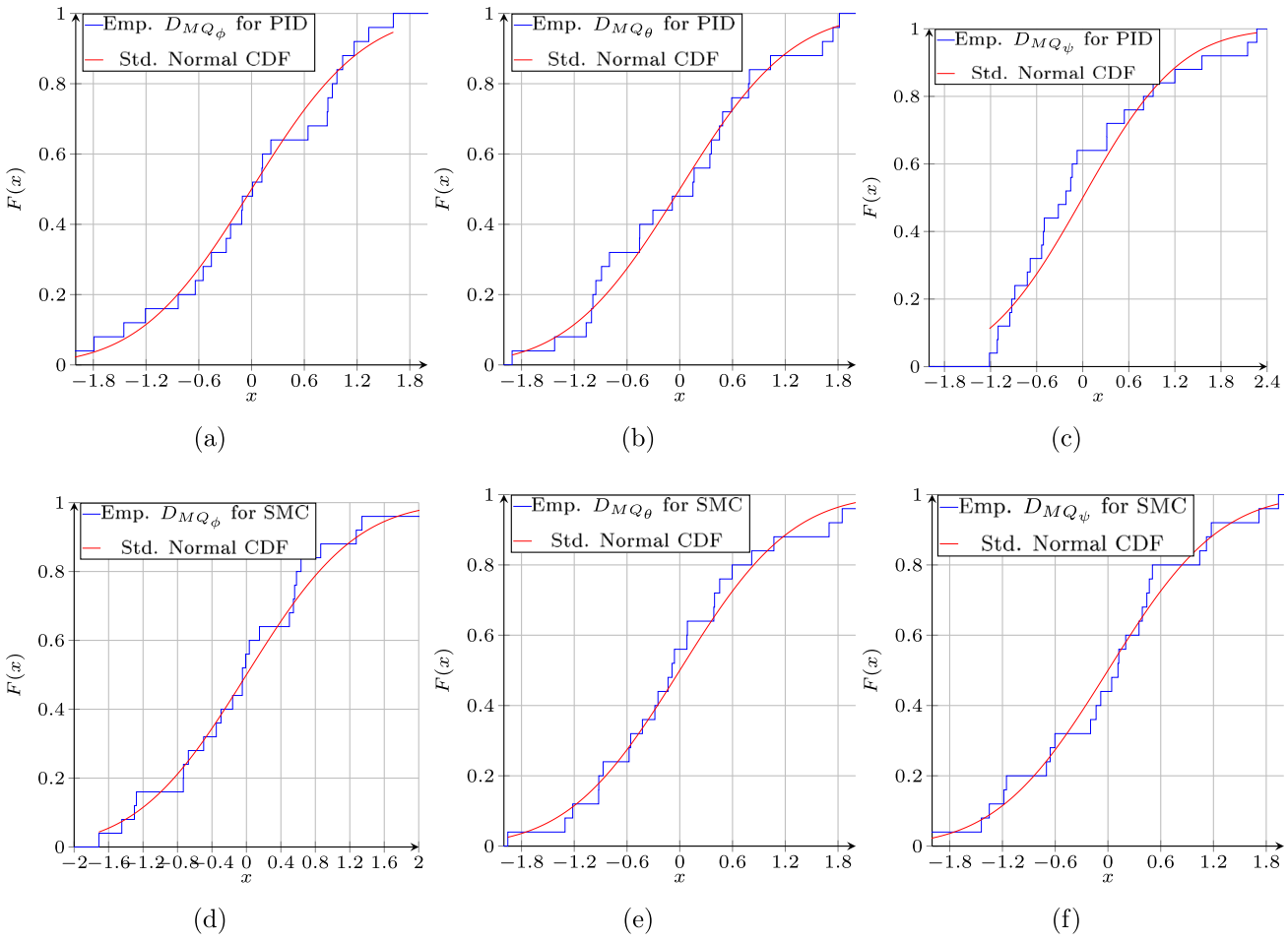

Fig. 15. Analysis of the cumulative probability density function for $M_F = 24\%$: (a) D_{MQ_ϕ} from PID, (b) D_{MQ_θ} from PID, (c) D_{MQ_ψ} from PID, (d) D_{MQ_ϕ} from SMC, (e) D_{MQ_θ} from SMC, and (f) D_{MQ_ψ} from SMC. (For interpretation of the references to color in this figure legend, the reader is referred to the web version of this article.)

Table 6
Confidence interval with 95% significance for 25 simulations of $D_{MQ_{(\phi)(\theta)(\psi)}}$.

Angle	Type	M_F											
		8				16				24			
		μ	σ	C_i		μ	σ	C_i		μ	σ	C_i	
ϕ	PID	1.99	0.054	1.97	2.01	2.01	0.072	1.98	2.04	2.33	0.097	2.29	2.37
	SMC	2.68	0.075	2.64	2.71	2.68	0.052	2.65	2.70	2.71	0.072	2.68	2.74
θ	PID	3.74	0.082	3.71	3.78	9.39	0.044	9.37	9.41	16.27	0.072	16.24	16.30
	SMC	4.42	0.040	4.40	4.43	4.33	0.036	4.32	4.35	4.21	0.049	4.19	4.23
ψ	PID	1.31	0.058	1.29	1.34	0.64	0.034	0.63	0.65	37.79	11.973	32.85	42.73
	SMC	0.59	0.065	0.56	0.62	0.70	0.056	0.68	0.73	3.43	0.589	3.19	3.68

ten times lower than that of the PID, with reduced variability. These results statistically reinforce the effectiveness of the proposed control strategy.

In general, scenarios with failures of $M_F \geq 10\%$ demonstrated significant attenuation at angles θ and ψ. The values of D_{MQ_θ} remained below 5°, allowing better control of the aircraft even with a faulty propeller. By setting $\gamma = 0.5°$ to ensure the attenuation of failure effects and considering the angle θ as the most critical parameter, the SMC control meets the condition $D_{MQ_\theta} < \gamma$ for failures with $M_F \geq 10\%$. Therefore, the SMC control can be experimentally validated on the test platform, as proposed in the methodology.

4.3.1. Validation of the auxiliary control on the test platform

Following the analysis of the simulator tests and the validation of the results obtained on the test platform with PID control, tests with SMC control can be conducted on the platform to validate performance in scenarios involving failures in one of the actuators. Table 7 presents the values $D_{MQ_{(\phi)(\theta)(\psi)}}$ and $E_{Q_{(\phi)(\theta)(\psi)}}$ obtained from both the simulator and the test platform using the SMC control. The blue values indicate the smallest difference between the simulator and the platform results, while the red values indicate the largest difference.

For angle ϕ, the smallest difference between the simulated and practical values D_{MQ_ϕ} occurred at $M_F = 28\%$, with a variation of 0.4°, while the largest difference was 1.7° at $M_F = 14\%$. In all experiments, the practical values D_{MQ_ϕ} were lower compared to the simulated ones. The value of E_{q_ϕ} remained below 7% in all tests, demonstrating the simulator's ability to accurately represent the quadcopter system.

For angle θ, the smallest difference between the simulated and practical values D_{MQ_θ} was 0.1° at $M_F = 24\%$, while the largest difference occurred at $M_F = 20\%$, with a variation of 1.3°. Furthermore, at $M_F =$

Table 7
Results obtained for $D_{MQ_{(\phi)(\theta)(\psi)}}$ and $E_{Q_{(\phi)(\theta)(\psi)}}$ through the simulator and the test platform using the SMC control with $\eta = 10\%$.

Angle	Type	M_F														
		2	4	6	8	10	12	14	16	18	20	22	24	26	28	30
ϕ	Sim [°]	2.6	2.5	2.6	2.7	2.5	2.7	**2.6**	2.6	2.6	2.6	2.6	2.5	2.5	**2.6**	2.6
	Plat [°]	1.9	1.7	1.9	1.3	1.7	1.4	**0.9**	1.1	0.9	1.0	1.4	1.5	1.6	**2.2**	2.1
	E_{q_ϕ} [%]	2.5	3.0	2.5	5.1	2.9	4.7	6.2	5.4	6.0	5.8	4.2	3.8	3.4	1.7	1.9
θ	Sim [°]	4.4	4.3	4.3	4.4	4.3	4.3	4.2	4.3	4.3	**4.2**	4.2	**4.1**	4.2	4.1	4.1
	Plat [°]	3.9	4.1	3.7	4.0	3.7	4.1	3.5	3.7	3.6	**5.5**	4.3	**4.2**	4.0	4.9	4.6
	E_{q_θ} [%]	2.0	0.9	2.1	1.2	1.9	0.8	2.4	2.0	2.3	4.3	0.6	0.1	0.5	2.7	1.6
ψ	Sim [°]	0.9	**0.9**	0.5	0.5	0.5	0.6	0.6	0.7	0.8	0.8	1.3	3.0	8.3	**16.8**	19.3
	Plat [°]	2.0	**1.8**	1.6	1.6	1.8	1.8	1.8	1.7	1.6	3.6	5.3	5.3	17.0	**26.9**	22.1
	E_{q_ψ} [%]	0.6	0.4	0.5	0.6	0.6	0.6	0.6	0.5	0.4	1.5	2.2	1.2	4.6	5.1	1.4

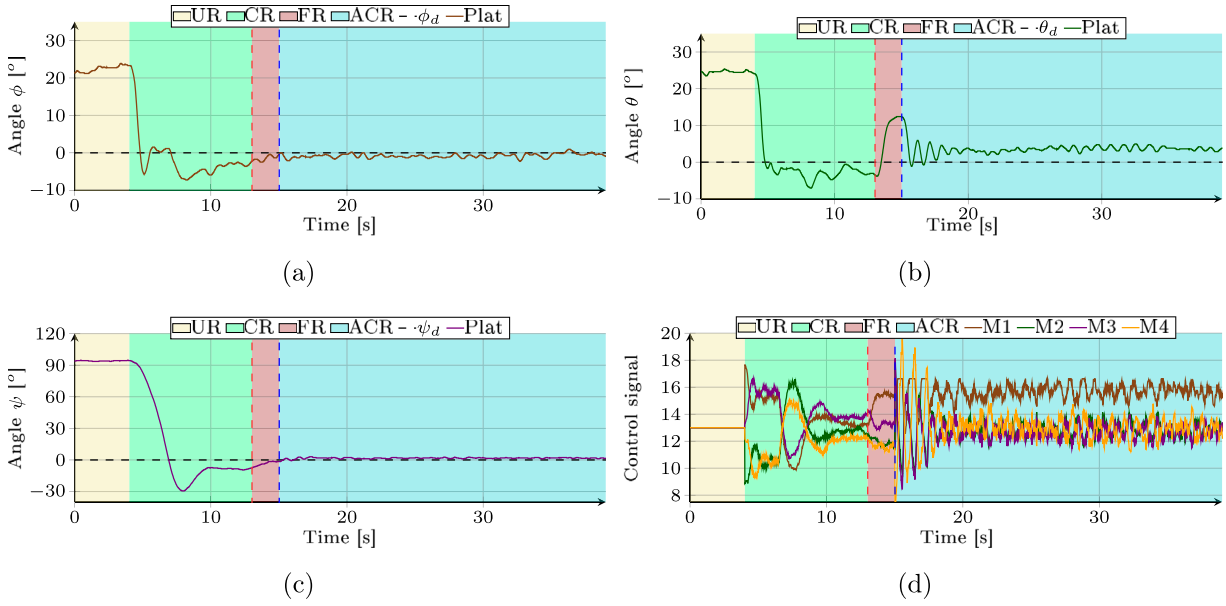

Fig. 16. Results obtained using SMC control on the platform for $M_F = 14\%$: (a) ϕ, (b) θ, (c) ψ and (d) control signals.

8%, the value D_{MQ_θ} obtained on the bench with the SMC control was 4.0°, lower than the value obtained with the PID control, indicating that the SMC control performs better for failures of this magnitude. The E_{q_θ} remained below 5% in all experiments, demonstrating the accuracy of the simulator in representing the quadcopter system.

For angle ψ, the smallest difference between the simulated and practical values D_{MQ_ψ} was 0.9° at $M_F = 4\%$, while the largest difference occurred at $M_F = 28\%$, with a variation of 9.9°. This variation in $M_F = 28\%$ may have been influenced by external factors in the practical experiment, since the value of D_{MQ_ψ} did not follow the growth pattern observed in similar scenarios. The E_{q_ψ} remained below 6% in all experiments. Fig. 16 presents the results of the SMC control for $M_F = 14\%$. Fig. 16(a) shows that the SMC control kept the angle ϕ stable at approximately 0°. Fig. 16(b) shows the behavior of the angle θ, where it is observed that, after switching to the SMC control, the amplitude was reduced, demonstrating the desired performance for this variable.

Fig. 16(c) shows the behavior of the angle ψ, which remains stable with oscillations around approximately 0° after the transition to the SMC control. Fig. 16(d) presents the control signals sent by the controller to the four ESCs. It can be seen that, in the CR region, the PID control adjusts these signals to stabilize the system, keeping them nearly constant after 10 s. When failure is introduced in the FR region, the PID control modifies these signals in an attempt to correct the error, and in the ACR region, the SMC control takes over, as indicated by the switching of the signals to restore the stability of the quadcopter.

Fig. 17 presents the results obtained for the SMC control with $M_F = 20\%$. Fig. 17(a) shows that the SMC control kept the angle ϕ stable. In Fig. 17(b), it is observed that the failure initially caused the angle θ to vary by more than 20.0°. After switching to the SMC control, the amplitude of this angle was reduced to approximately 4.0°, representing an attenuation of approximately 80% compared to the peak observed at the end of the FR region and the beginning of the ACR region.

Fig. 17(c) presents the behavior of the angle ψ, where after the failure in M_1, it begins to diverge, but stabilizes with the SMC control. In Fig. 17(d), the control signals sent by the controller to the four ESCs indicate that, at the beginning of the ACR region, the S_{M1} signal is saturated at $a_{max} \approx 18$, preventing the faulty motor from receiving high-amplitude signals that could exacerbate failure in real scenarios. Fig. 18 presents the results for the SMC control with $M_F = 26\%$. Fig. 18(a) shows that although the SMC control kept the ϕ angle stable, it starts to be affected, diverging approximately 10.0° from the desired value in the FR region. Fig. 18(b) shows that the failure caused a variation of nearly 30.0° in the angle θ, which was attenuated to approximately 5.0° in the region ACR with the use of auxiliary control.

Fig. 18(c) presents the behavior of the angle ψ, where the failure in M_1 causes a variation, but with the activation of the SMC control, the rate of increase is reduced. After approximately 3 s with active SMC control, the angle ψ stabilizes and begins to return to the desired value of $\psi_d = 0°$. Fig. 18(d) presents the control signals sent to the four ESCs, indicating that, at the beginning of the ACR region, the S_{M1} signal is saturated at $a_{max} \approx 20$ and remains at this value until the system can restore the angle ψ to its desired value.

Fig. 19 presents the phase planes for the experiment with $M_F = 26\%$, highlighting the behavior of the error and its derivative for each

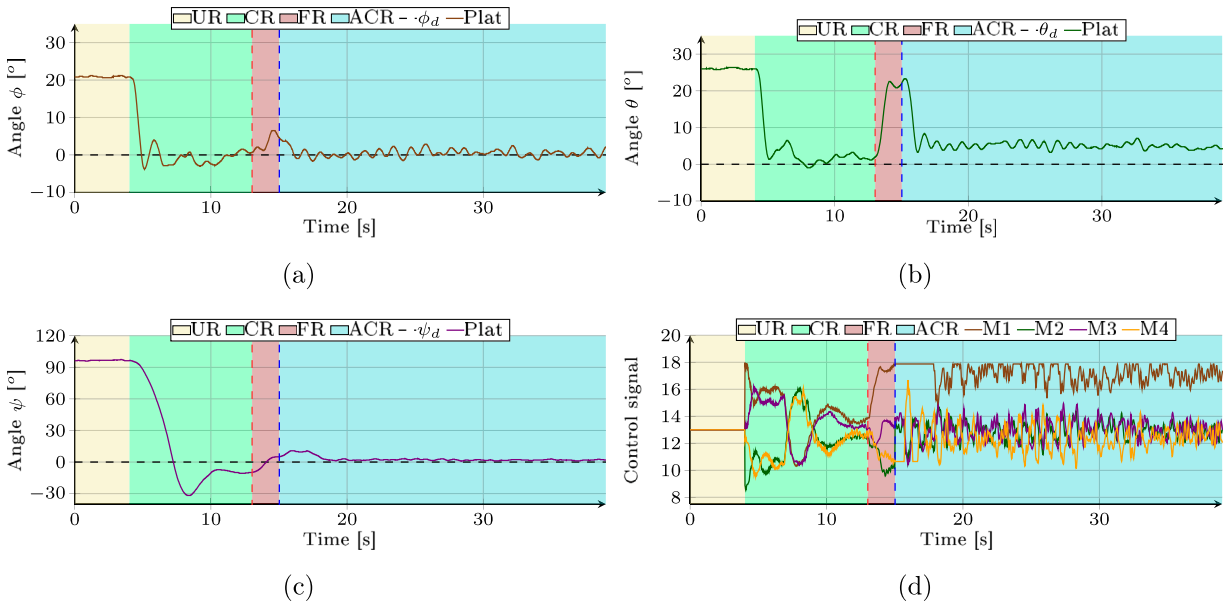

Fig. 17. Results obtained using SMC control on the platform for $M_F = 20\%$: (a) ϕ, (b) θ, (c) ψ and (d) control signals.

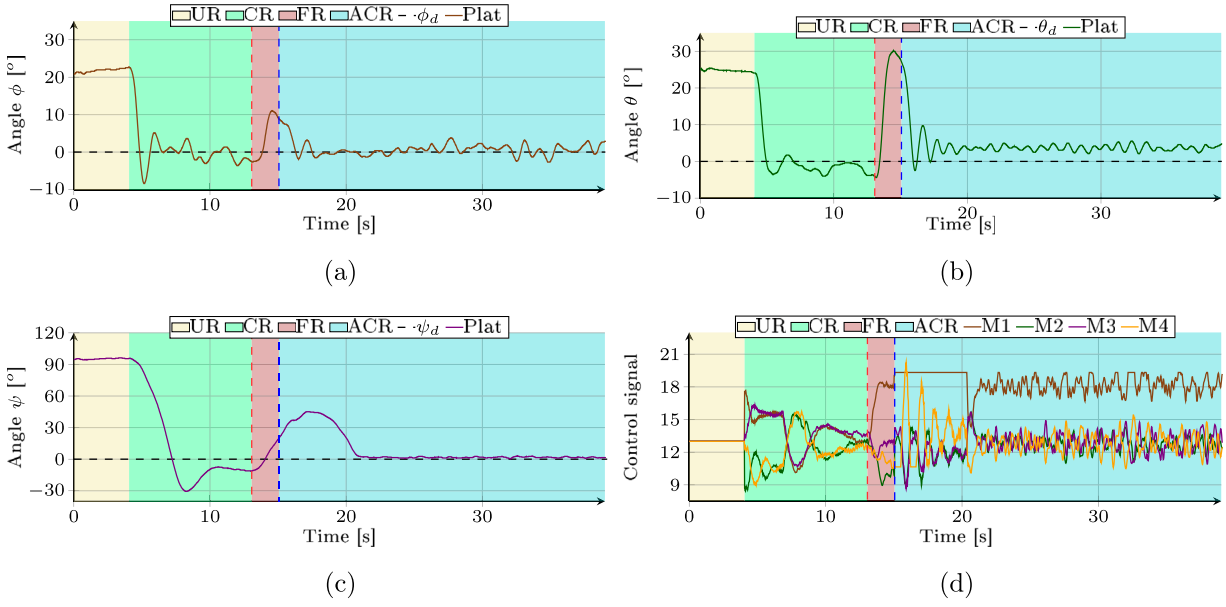

Fig. 18. Results obtained using SMC control on the platform for $M_F = 26\%$: (a) ϕ, (b) θ, (c) ψ and (d) control signals.

angle. The yellow, green, red, and turquoise curves correspond to the UR, CR, FR, and ACR regions, respectively. In Fig. 19(a), the phase plane for the angle ϕ is shown. After the start of the CR region, the curve shifts from $e_\phi(t) \approx -22°$ to $\dot{e}_\phi(t) \approx 0°/s$ to oscillate between $e_\phi(t) \pm -5°$ and $\dot{e}_\phi(t) \pm 15°/s$. When failure is introduced, $\dot{e}_\phi(t)$ reaches approximately $-30°/s$, driving $e_\phi(t)$ to approximately $-10°$ at the end of the FR region. In the ACR region, the signal returns to oscillating between $e_\phi(t) \pm -5°$ and $\dot{e}_\phi(t) \pm 15°/s$.

Fig. 19(b) displays the phase plane for the angle θ. In the CR region, the curve starts from $e_\theta(t) \approx -25°$ with $\dot{e}_\theta(t) \approx 0°/s$ and oscillates between $e_\theta(t) \pm -5°$ and $\dot{e}_\theta(t) \pm 10°/s$. When failure is introduced, $\dot{e}_\theta(t)$ reaches approximately $-60°/s$, twice the value observed for $\dot{e}_\phi(t)$, significantly increasing the error to $e_\theta(t) \approx -30°$ in the FR region. In the ACR region, the SMC control causes the states $e_\theta(t)$ and $\dot{e}_\theta(t)$ to follow a spiral trajectory of damped direction, with $e_\theta(t)$ oscillating between $-6°$ and $-4°$ and $\dot{e}_\theta(t)$ between $\pm 12°/s$.

Fig. 19(c) presents the phase plane for the angle ψ. In the CR region, the curve progresses from $e_\psi(t) \approx -100°$ with $\dot{e}_\psi(t) \approx 0°/s$ to $e_\psi(t) \approx 12°$ and $\dot{e}_\psi(t) \approx -3°/s$, indicating that the error has not yet been fully eliminated by the integrative component of the PID controller. When failure is introduced, $\dot{e}_\psi(t)$ reaches approximately $-20°/s$, a lower value than observed for $\dot{e}_\phi(t)$ and $\dot{e}_\theta(t)$, resulting in $e_\psi(t) \approx -20°$ at the end of the FR region. In the ACR region, the SMC control drives the states $e_\psi(t)$ and $\dot{e}_\psi(t)$ toward the sliding surface, and upon reaching it, both converge to approximately $0°$ and $0°/s$, respectively.

4.3.2. Analysis under asymmetric inertia matrix and non-equilibrium initial conditions

To evaluate the resilience of the auxiliary control system under more realistic conditions, tests were conducted considering two additional scenarios: (i) asymmetry in the inertia matrix, with $J_x \neq J_y$, and (ii) operation outside the equilibrium region. For the first case, $J_x = 1.2J_y$ was adopted to simulate the effect of a nonuniform mass

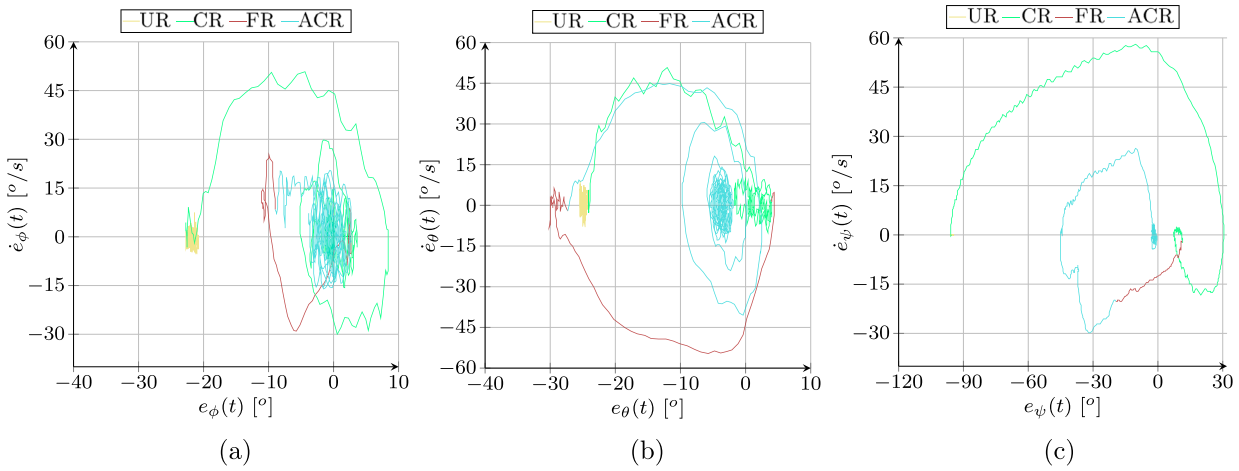

Fig. 19. Phase plan for the test platform experiment with $M_F = 26\%$: (a) ϕ, (b) θ, and (c) ψ. (For interpretation of the references to color in this figure legend, the reader is referred to the web version of this article.)

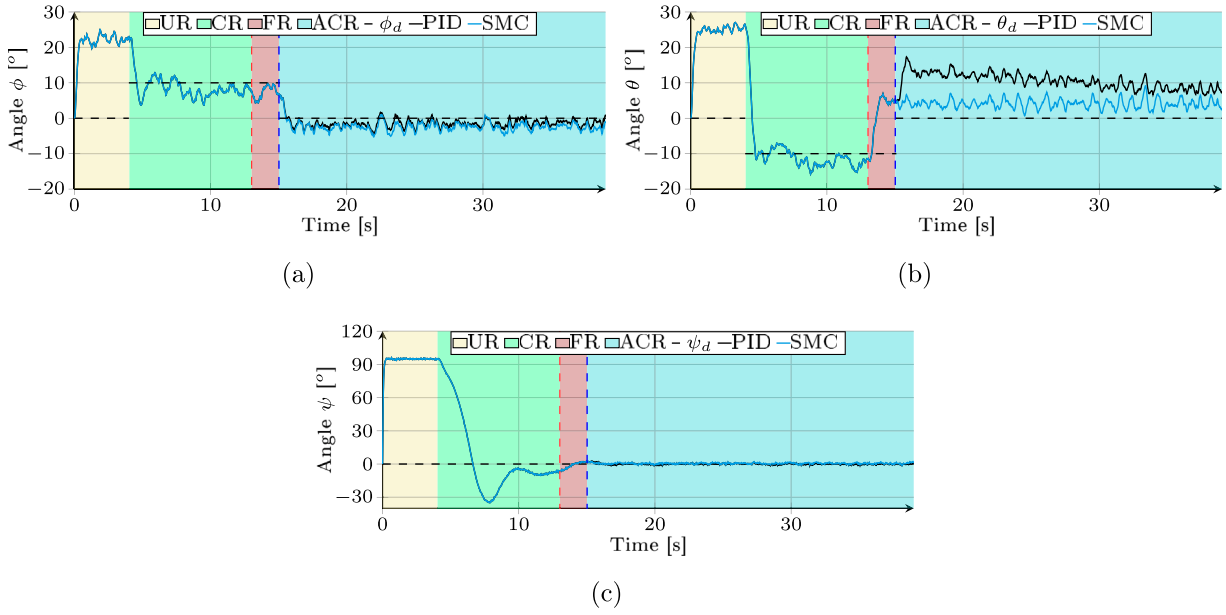

Fig. 20. Simulation analysis for $Jx = 1.2J_y$ and $M_F = 18\%$ for PID control and SMC control: (a) ϕ, (b) θ and (c) ψ.

distribution, which is common in real quadcopters. For the second, the desired angles were initially set at $\phi_d = 10°$ and $\theta_d = -10°$, removing the vehicle from the equilibrium point. Once failure is detected, the auxiliary control system is activated, and the desired angles are reset to $\phi_d = \theta_d = 0°$ to stabilize the aircraft under fault conditions.

Fig. 20 illustrates the dynamic response of angles ϕ, θ, and ψ under a fault condition with $M_F = 18\%$, for both PID and SMC controllers. It can be observed that the angles ϕ and ψ exhibit similar behavior in both cases. However, despite the asymmetric inertia and the system starting from a tilted configuration, the auxiliary controller effectively mitigated the impact of failure on angle θ, maintaining the stability of the aircraft.

Table 8 presents the values of $D_{MQ_{(\phi)(\theta)(\psi)}}$ obtained from simulations with $J_x = J_y$ and $J_x = 1.2J_y$, at different fault levels. The results indicate that the SMC controller maintained consistent performance for θ even under inertia asymmetry, strengthening its structural resilience. For ψ, the SMC controller prevented the instability observed with the PID controller at $M_F = 24\%$, where the error reached 42.0° with PID, compared to only 1.8° with SMC.

These results suggest that the proposed controller maintains stability even outside the vicinity of the equilibrium point, indicating a sufficiently large domain of attraction to accommodate significant perturbations in the initial conditions. Although no formal proof of global stability was performed, the simulation results demonstrate that the system remains stable under a wide range of inertial and angular disturbances, reinforcing the practical applicability of the proposed method.

5. Discussion

The empirical and computational foundation developed throughout this study supports a structured analysis of the performance of the proposed sliding mode control strategy. This section discusses the main advances in relation to the specialized literature, the challenges faced, and the operational conditions that define the applicability of the system. Finally, it presents methodological limitations and opportunities for improvement, along with directions for future research.

Although sliding mode control forms the basis of the implemented solution, it is not the central contribution of this work. Instead, it serves as a component within a wider resilient control strategy. The originality of the proposed approach lies in the explicit redistribution of control

Table 8
Comparison between the $D_{MQ_{(\phi)(\theta)(\psi)}}$ obtained with the PID control and the proposed auxiliary control, for simulations with $J_x = J_y$ and $J_x = 1.2J_y$.

Angle	Type	M_F												
		0	2	4	6	8	10	12	14	16	18	20	22	24
ϕ	PID	2.1	2.1	2.0	2.1	2.3	2.1	2.1	2.1	2.1	**1.9**	2.2	2.1	**2.4**
	SMC	2.7	2.6	2.6	2.7	2.8	2.6	2.7	2.5	2.6	**2.6**	2.7	2.6	**2.6**
θ	PID	2.4	1.8	1.6	2.5	3.6	**4.8**	6.0	7.5	9.1	10.7	12.3	14.1	**15.9**
	SMC	4.6	4.7	4.3	4.3	4.4	**4.3**	4.3	4.3	4.3	4.3	4.2	4.2	**4.1**
ψ	PID	1.9	1.9	1.6	1.5	1.2	1.0	0.8	0.6	0.6	0.6	**0.7**	1.6	**42.0**
	SMC	1.1	1.5	1.4	0.9	0.7	0.6	0.6	0.7	0.7	0.7	**0.7**	0.9	**1.8**

efforts under partial actuator failures, including the deactivation of the tilt contribution from the faulty propulsor and the dynamic reallocation of the remaining torques, ensuring system stability even under severe asymmetries. The sign function is replaced by a saturation function to smooth the control action and ensure compatibility with real actuators. The entire framework can be adapted to alternative control laws that meet the established criteria for convergence and robustness, highlighting the generality and practical applicability of the proposed solution.

5.1. Main contributions and comparison with the literature

The development of techniques to mitigate the impacts of propeller failures in quadcopters has been the focus of numerous studies, given the importance of maintaining the stability and safety of these aircraft in adverse situations. This work presents a significant advancement in this field by proposing a sliding mode control (SMC) approach to stabilize quadcopters during propeller failures. The results demonstrated a reduction of more than 80% in the negative effects caused by loss of power in one of the propellers, particularly in controlling the angles ϕ, θ, and ψ. The ability of SMC to maintain aircraft stability even with failures of up to 30% indicates its robustness and efficiency, positioning it as a promising solution for practical applications where safety and reliability are paramount.

In terms of alignment with the existing literature, this work is consistent with the findings of Baldini et al. [28], who also investigated advanced control techniques for propeller failures. Both studies employ control strategies to mitigate the effects of quadcopters failures, demonstrating the effectiveness of these approaches in maintaining the stability of the aircraft. However, while Baldini et al. focus on fault detection and fault-tolerant control without providing a specific success metric in percentage terms, this study extends the applicability of SMC control, showing its effectiveness under more severe conditions, with failures up to 30%. This extension of operational conditions represents a significant contribution to the field, as it expands the applicability limits of quadcopters under adverse conditions. Furthermore, unlike the approach proposed by Merheb et al. [30], which relies on modifying the center of mass to compensate for failure, the SMC approach does not require structural modifications of the aircraft, thus avoiding the addition of weight and preserving vehicle autonomy.

However, significant divergences also emerge compared to other studies. For example, the works by Wu et al. [26] and Mueller & D'Andrea [24] choose to sacrifice control of the angle ψ, allowing the aircraft to rotate freely around the axis z during failures, at the cost of increasing the load on the other actuators. Although this approach is effective in maintaining flight stability in critical situations, it can compromise maneuverability and overall control of the aircraft, especially in environments where precise control of all angles is important. In contrast, the proposed study demonstrated that SMC control is capable of maintaining complete control, including angle ψ, without requiring such trade-offs, which can be vital in complex operations or in confined spaces.

The main gap identified in the literature is related to the difficulty of maintaining full control of the quadcopter during significant propeller failures without resorting to structural modifications or sacrificing some degree of control. The contribution of this work lies precisely in overcoming this limitation by providing a solution that preserves the vehicle's structural integrity while ensuring its stability and control, even in failure scenarios. However, this work is not without challenges and limitations. One of the difficulties encountered was the need to precisely calibrate the SMC control for different failure scenarios, which requires detailed knowledge of the aircraft dynamics and the operational limits of the actuators. Furthermore, while SMC control is effective, it can exhibit oscillations and chattering behavior in abrupt failure situations, which may compromise control precision.

5.2. Validation, applicability and operational constraints

However, this work is not without challenges and limitations. One of the main difficulties was the need for precise calibration of the sliding mode control in different failure scenarios, which requires detailed knowledge of the aircraft dynamics and the operational limits of the actuators. Moreover, although the SMC strategy proved effective, it can exhibit oscillations and abrupt switching behavior under sudden failure conditions, potentially compromising control accuracy. Operational aspects such as the energy impact of thrust redistribution, the physical constraints of the experimental platform, and the tolerance of the actuators to saturation also represent critical factors in evaluating the applicability of the proposed system.

In this context, the use of the test platform proposed in [52], which limits the rotation angles to $\phi = \pm 25°$ and $\theta = \pm 25°$, does not compromise the validity of the stability results. This choice was driven by operational safety concerns and prototype instrumentation limitations. However, the observed results are not artificially enhanced by these limitations. The simulations performed with the full dynamic model, without any constraints on the rotation angles, exhibited behavior consistent with the experimental data, as illustrated by the cyan curves in Figs. 13 and 14. Therefore, the stability achieved is not a consequence of the physical limitations of the test platform, but rather of the ability of the auxiliary control system to mitigate failure effects under broader operating conditions.

In the most severe scenario considered in this study, corresponding to a failure of $M_F = 30\%$, the remaining three propellers must compensate by redistributing approximately 10% additional power relative to nominal operation. For this compensation to be feasible, each propeller must operate under normal flight conditions with at least a 10% margin below its actuator saturation threshold. This margin is consistent with typical operating regimes of commercial quadcopters, in which motors rarely run continuously at full power due to the demands of fine stability and hovering maneuvers [57,58]. Consequently, the proposed power redistribution strategy remains within the physical limits of the actuators, provided that this operational reserve is accounted for in the design of the propulsion system. Although a formal analytical proof is not presented, saturation conditions can be avoided for $M_F \leq 30\%$ as long as the required power margin is ensured in advance.

The methodology adopted in this study assumes partial failures in a single propeller, with progressive performance losses not exceeding

30% of nominal power. This threshold was defined based on the progressive degradations observed in the power control units, particularly linked to the thermal deterioration of the ESC and gradual rotor faults, in which the motors continue to operate partially before complete shutdown [59,60]. Within this range, simulations indicate that the sliding mode control system maintains vehicle stability and provides sufficient time for safe landing maneuvers.

However, no experimental measurements of electrical current, temperature, or energy consumption were conducted under failure conditions, which limits the assessment of the system's thermal and electrical reliability in real-world scenarios. Furthermore, the proposed strategy has not been validated for cases of total failure (100%) or multiple simultaneous failures, which would require additional control mechanisms or mechanical redundancy. Therefore, the feasibility of the system remains restricted to single and partial failure scenarios. Determining the maximum cumulative failure threshold that preserves global stability requires further studies, including thermal modeling, torque analysis under variable load conditions, and integration with fault prediction mechanisms.

Another relevant aspect regarding the generalization of the proposed approach concerns the representation of vehicle orientation. This study adopts Tait–Bryan angles to describe the attitude of the aircraft, which is adequate for the operating regimes evaluated, where the inclination angles remain significantly far from the critical condition $\theta = \pm 90°$. However, this parameterization has well-known limitations, such as the gimbal lock, which may occur during acrobatic maneuvers or extreme tilting. For applications involving full rotations or inverted flight, it is recommended to adopt a representation based on quaternions, which ensures mathematical continuity and eliminates the singularities associated with Euler angle parameterization [61,62].

Although the experimental platform used in this study does not allow maneuvers with angles approaching $\pm 90°$, the transition to a quaternion-based representation is already considered promising. Future implementations of the auxiliary control system may adopt quaternions to ensure compatibility with more aggressive flight scenarios. The application of sliding mode control within the quaternion space is feasible and can be incorporated without loss of generality, provided that the error signals and sliding surfaces are properly reformulated in this new reference frame. This mathematical enhancement, along with complementary investigations on parametric uncertainties and alternative control strategies, defines the scope of the perspectives discussed in the following section.

5.3. Limitations and perspectives for future research

In addition to the aforementioned mathematical adaptations, another critical aspect to be further explored involves the influence of parametric uncertainties on controller performance. Future investigations will include sensitivity analyses to quantify the impact of such uncertainties. Variations in parameters such as mass, moment of inertia, motor efficiency, and aerodynamic coefficients will be evaluated to understand how these fluctuations affect system stability and attitude tracking accuracy. This approach will enable a more precise estimation of operational margins and enhance the resilience of the control strategy under real-world conditions, where minor structural and environmental variations are unavoidable. The implementation of these analyses is planned as a complementary stage of this study.

Furthermore, it is acknowledged that SMC, although well established in the fault-tolerant control literature, is not the only recent advancement in the field. Modern techniques such as adaptive control, reinforcement learning, and hybrid architectures that incorporate active disturbance rejection and multilayer neurocontrol have been successfully explored in high-order nonlinear systems subject to uncertainties. In this study, SMC was selected because of its structural simplicity, immediate applicability to the experimental platform, and proven resilience to abrupt disturbances. However, comparative evaluations involving alternative fault-tolerant control strategies represent a promising direction for future research, both in simulation and in practical implementation. Systematic assessments involving approaches such as self-tuning adaptive control and deep reinforcement learning will be considered in subsequent stages to extend the applicability of the proposed system to broader levels of dynamic uncertainty and operational complexity.

To overcome these limitations, future research could explore the integration of SMC control with machine learning techniques, allowing the system to adapt more efficiently to a broader range of failure conditions. Furthermore, implementing fault prediction mechanisms that allow SMC control to anticipate and mitigate impacts before they become critical could further enhance the system's robustness and reliability. The combination of these approaches could potentially set new standards for safety and performance in quadcopters, expanding their applications in areas where failure is not an option.

6. Conclusions

In this work, a sliding mode control (SMC) auxiliary system was developed and validated for quadcopters, focusing on mitigating the impacts of propeller failures. Given the importance of maintaining the stability of these aircrafts in adverse situations, the research concentrated on simulations and practical tests to evaluate the efficiency of SMC control in critical scenarios, such as a 30% power loss in one of the propellers. This study contributes to the literature by demonstrating the ability of SMC control to maintain aircraft stability under severe conditions without sacrificing control over any of the orientation angles.

The primary hypothesis of the study, which suggested that the SMC control would be capable of stabilizing the quadcopter in failure scenarios, was corroborated by the results obtained. The established objectives were fully achieved, as indicated by the validation of the nonlinear simulator and the convergence of the experimental results with the simulated ones, which showed differences of less than $E_{q_{global}} \leq 2°$ for the variables ϕ, θ and ψ. This consistent performance between simulations and practical tests confirms the robustness and efficiency of the proposed SMC control.

The most significant results include the reduction of more than 80% of the negative effects caused by power loss at the angle of θ, the preservation of control over the angles of ϕ and ψ, and the validation of the nonlinear simulator as an accurate tool for representing the dynamics of the system in failure scenarios. Therefore, it is concluded that the SMC control developed in this study is an efficient and robust solution to maintain the stability of quadcopters in propeller failure scenarios, with potential for real-world applications.

CRediT authorship contribution statement

Junio Santos Bulhões: Writing – review & editing, Writing – original draft, Visualization, Validation, Supervision, Software, Resources, Methodology, Investigation, Formal analysis, Data curation, Conceptualization. **Cristiane Lopes Martins:** Writing – review & editing, Writing – original draft, Visualization, Validation, Supervision, Software, Resources, Methodology, Investigation, Formal analysis, Data curation, Conceptualization. **Viviane M. Gomes Pacheco:** Writing – review & editing, Writing – original draft, Visualization, Validation, Software, Resources, Investigation, Formal analysis, Conceptualization. **Alana da Silva Magalhães:** Visualization, Validation, Supervision, Software, Project administration, Formal analysis, Conceptualization. **Clóves Gonçalves Rodrigues:** Writing – review & editing, Writing – original draft, Visualization, Validation, Methodology, Formal analysis, Conceptualization. **Antonio Paulo Coimbra:** Writing – review & editing, Writing – original draft, Visualization, Validation, Methodology, Formal analysis, Conceptualization. **Wesley Pacheco Calixto:** Writing – review & editing, Writing – original draft, Visualization, Validation, Supervision, Software, Resources, Methodology, Investigation, Formal analysis, Data curation, Conceptualization.

Declaration of competing interest

The authors declare that they have no known competing financial interests or personal relationships that could have appeared to influence the work reported in this paper.

Acknowledgments

The authors acknowledge the financial support provided by the Fundação para a Ciência e a Tecnologia (FCT/Portugal), I.P., under project UIDB/00048/2020 (DOI: 10.54499/UIDB/00048/2020), and the National Council for Scientific and Technological Development (CNPq/Brazil) for supporting this research through a Research Productivity Fellowship (Grant No. 301644/2022-5). Furthermore, the authors express their gratitude to the Brazilian Federal Agency for Support and Evaluation of Graduate Education (CAPES/Brazil) for the postdoctoral fellowship support (Grant Nos. 88887.927817/2023-00, 88887.985910/2024-00). The authors thank LaMCAD/UFG for the computational resources that supported this research.

Data availability

The data are available on Code Ocean with the corresponding DOI: 10.24433/CO.3597880.v1.

References

[1] Q.C. Pham, R. Madhavan, L. Righetti, W. Smart, R. Chatila, The impact of robotics and automation on working conditions and employment [Ethical, Legal, and Societal Issues], IEEE Robot. Autom. Mag. 25 (2) (2018) 126–128, http://dx.doi.org/10.1109/MRA.2018.2822058.

[2] M. Samir, S. Sharafeddine, C.M. Assi, T.M. Nguyen, A. Ghrayeb, UAV trajectory planning for data collection from time-constrained IoT devices, IEEE Trans. Wirel. Commun. 19 (1) (2019) 34–46, http://dx.doi.org/10.1109/TWC.2019.2940447.

[3] A. Alkamachi, E. Ercelebi, H∞ control of an overactuated tilt rotors quadcopter, J. Cent. South Univ. 25 (3) (2018) 586–599, http://dx.doi.org/10.1007/s11771-018-3763-2.

[4] M. Hassanalian, A. Abdelkefi, Classifications, applications, and design challenges of drones: A review, Prog. Aerosp. Sci. (ISSN: 0376-0421) 91 (2017) 99–131, http://dx.doi.org/10.1016/j.paerosci.2017.04.003, URL https://www.sciencedirect.com/science/article/pii/S0376042116301348.

[5] K.H. Kindervater, The emergence of lethal surveillance: Watching and killing in the history of drone technology, Secur. Dialogue 47 (3) (2016) 223–238, http://dx.doi.org/10.1177/0967010615616011.

[6] T. Krajník, V. Vonásek, D. Fišer, J. Faigl, AR-drone as a platform for robotic research and education, in: International Conference on Research and Education in Robotics, Springer, 2011, pp. 172–186, http://dx.doi.org/10.1007/978-3-642-21975-7_16.

[7] A.E. Holton, S. Lawson, C. Love, Unmanned Aerial Vehicles: Opportunities, barriers, and the future of "drone journalism", Journal. Pr. 9 (5) (2015) 634–650, http://dx.doi.org/10.1080/17512786.2014.980596.

[8] V. Puri, A. Nayyar, L. Raja, Agriculture drones: A modern breakthrough in precision agriculture, J. Stat. Manag. Syst. 20 (4) (2017) 507–518, http://dx.doi.org/10.1080/09720510.2017.1395171.

[9] U.R. Mogili, B. Deepak, Review on application of drone systems in precision agriculture, Procedia Comput. Sci. 133 (2018) 502–509, http://dx.doi.org/10.1016/j.procs.2018.07.063.

[10] S.H. Alsamhi, O. Ma, M.S. Ansari, S.K. Gupta, Collaboration of drone and internet of public safety things in smart cities: An overview of qos and network performance optimization, Drones 3 (1) (2019) 13, http://dx.doi.org/10.3390/drones3010013.

[11] J. Jiménez López, M. Mulero-Pázmány, Drones for conservation in protected areas: present and future, Drones 3 (1) (2019) 10, http://dx.doi.org/10.3390/drones3010010.

[12] S.H. Seo, J. Won, E. Bertino, Y. Kang, D. Choi, A security framework for a drone delivery service, in: Proceedings of the 2Nd Workshop on Micro Aerial Vehicle Networks, Systems, and Applications for Civilian Use, 2016, pp. 29–34, http://dx.doi.org/10.1145/2935620.2935629.

[13] X. Yu, Z. Liu, Y. Zhang, Fault-tolerant formation control of multiple UAVs in the presence of actuator faults, Internat. J. Robust Nonlinear Control 26 (12) (2016) 2668–2685, http://dx.doi.org/10.1002/rnc.3467.

[14] A. Nemati, R. Kumar, M. Kumar, Stabilizing and control of Tilting-Rotor quadcopter in case of a propeller failure, in: Dynamic Systems and Control Conference, Vol. 1, American Society of Mechanical Engineers, 2016, V001T05A005, http://dx.doi.org/10.1115/DSCC2016-9897.

[15] S. Hanssen, Drone Class: Keeping coursework current as technology advances, Community Coll. J. Res. Pr. 40 (10) (2016) 871–874, http://dx.doi.org/10.1080/10668926.2015.1102105.

[16] M. Krey, Cure for health care? Using drone technology in hospital Processes-An explorative analysis, in: Third International Congress on Information and Communication Technology, Springer, 2019, pp. 13–24, http://dx.doi.org/10.1007/978-981-13-1165-9_2.

[17] A. Panta, S. Watkins, R. Clothier, Dynamics of a small unmanned aircraft parachute system, J. Aerosp. Technol. Manag. 10 (2018) http://dx.doi.org/10.5028/jatm.v10.752.

[18] B. Wang, Y. Zhang, An adaptive fault-tolerant sliding mode control allocation scheme for multirotor helicopter subject to simultaneous actuator faults, IEEE Trans. Ind. Electron. 65 (5) (2018) 4227–4236, http://dx.doi.org/10.1109/TIE.2017.2772153.

[19] J. Lee, D. Shin, H. Ryu, D. Lee, D.H. Shim, Fault tolerant adaptive control using time delay control scheme under motor faults of octocopter, in: 2018 7th International Conference on Systems and Control, ICSC, IEEE, 2018, pp. 123–128, http://dx.doi.org/10.1109/ICoSC.2018.8587803.

[20] S. Zeghlache, H. Mekki, A. Bouguerra, A. Djerioui, Actuator fault tolerant control using adaptive RBFNN fuzzy sliding mode controller for coaxial octorotor UAV, ISA Trans. (ISSN: 0019-0578) 80 (2018) 267–278, http://dx.doi.org/10.1016/j.isatra.2018.06.003.

[21] M.F. Santos, L.M. Honório, E.B. Costa, E.J. Oliveira, J.P. Portella Guedes Visconti, Active fault-tolerant control applied to a hexacopter under propulsion system failures, in: 2015 19th International Conference on System Theory, Control and Computing, ICSTCC, IEEE, 2015, pp. 447–453, http://dx.doi.org/10.1109/ICSTCC.2015.7321334.

[22] N.P. Nguyen, N. Xuan Mung, S.K. Hong, Actuator fault detection and fault-tolerant control for hexacopter, Sensors (ISSN: 1424-8220) 19 (21) (2019) 4721, http://dx.doi.org/10.3390/s19214721.

[23] H. Mazeh, J. Sahili, Fault-tolerant control of a multirotor unmanned aerial vehicle applying particle swarm optimization, in: 2019 7th International Conference on Robotics and Mechatronics (ICRoM), IEEE, 2019, pp. 619–624, http://dx.doi.org/10.1109/ICRoM48714.2019.9071861.

[24] M.W. Mueller, R. D'Andrea, Stability and control of a quadrocopter despite the complete loss of one, two, or three propellers, in: 2014 IEEE International Conference on Robotics and Automation, ICRA, IEEE, 2014, pp. 45–52, http://dx.doi.org/10.1109/ICRA.2014.6906588.

[25] Y.V. Morozov, Emergency control of a quadrocopter in case of failure of two symmetric propellers, Autom. Remote Control 79 (3) (2018) 463–478, http://dx.doi.org/10.1134/S0005117918030062.

[26] Y. Wu, K. Hu, X.M. Sun, Y. Ma, Nonlinear control of quadrotor for fault tolerance: A total failure of one actuator, IEEE Trans. Syst. Man Cybern.: Syst. 51 (5) (2021) 2810–2820, http://dx.doi.org/10.1109/TSMC.2019.2917050.

[27] W. Jung, H. Bang, Fault and failure tolerant model predictive control of quadrotor UAV, Int. J. Aeronaut. Space Sci. 22 (3) (2021) 663–675, http://dx.doi.org/10.1007/s42405-020-00331-1.

[28] A. Baldini, R. Felicetti, A. Freddi, S. Longhi, A. Monteriù, Actuator fault tolerant control of variable pitch quadrotor vehicles, IFAC-PapersOnLine 53 (2) (2020) 4095–4102, http://dx.doi.org/10.1016/j.ifacol.2020.12.2439.

[29] N.P. Nguyen, S.K. Hong, Fault diagnosis and Fault-Tolerant control scheme for quadcopter UAVs with a total loss of actuator, Energies (ISSN: 1996-1073) 12 (6) (2019) 1139, http://dx.doi.org/10.3390/en12061139.

[30] A.R. Merheb, H. Noura, F. Bateman, A novel emergency controller for quadrotor uavs, in: 2014 IEEE Conference on Control Applications, CCA, IEEE, 2014, pp. 747–752, http://dx.doi.org/10.1109/CCA.2014.6981430.

[31] M. Bhargavapuri, S.R. Sahoo, M. Kothari, et al., Robust nonlinear control of a variable-pitch quadrotor with the flip maneuver, Control Eng. Pract. 87 (2019) 26–42, http://dx.doi.org/10.1016/j.conengprac.2019.03.012.

[32] A. Chovancová, T. Fico, L. Chovanec, P. Hubinsk, Mathematical modelling and parameter identification of quadrotor (a survey), Procedia Eng. 96 (2014) 172–181, http://dx.doi.org/10.1016/j.proeng.2014.12.139.

[33] E. Paiva, J. Soto, J. Salinas, W. Ipanaqué, Modeling, simulation and implementation of a modified PID controller for stabilizing a quadcopter, in: 2016 IEEE International Conference on Automatica (ICA-ACCA), IEEE, 2016, pp. 1–6, http://dx.doi.org/10.1109/ICA-ACCA.2016.7778507.

[34] B.L. Stevens, F.L. Lewis, E.N. Johnson, Aircraft Control and Simulation: Dynamics, Controls Design, and Autonomous Systems, John Wiley & Sons, 2015, http://dx.doi.org/10.1002/9781119174882.

[35] D. Kleppner, R. Kolenkow, An Introduction to Mechanics, second ed., Cambridge University Press, 2013, http://dx.doi.org/10.1017/CBO9781139013963.

[36] P.H. Zipfel, Modeling and Simulation of Aerospace Vehicle Dynamics, third ed., American Institute of Aeronautics and Astronautics, 2014, http://dx.doi.org/10.2514/4.102509.

[37] Z. Benić, P. Piljek, D. Kotarski, Mathematical modelling of unmanned aerial vehicles with four rotors, Interdiscip. Descr. Complex Syst.: INDECS 14 (1) (2016) 88–100, http://dx.doi.org/10.7906/indecs.14.1.9.

[38] D. Gheorghiță, I. Vîntu, L. Mirea, C. Brăescu, Quadcopter control system, in: 2015 19th International Conference on System Theory, Control and Computing, ICSTCC, IEEE, 2015, pp. 421–426, http://dx.doi.org/10.1109/ICSTCC.2015.7321330.

[39] M. Hancer, R. Bitirgen, I. Bayezit, Designing 3-DOF hardware-in-the-loop test platform controlling multirotor vehicles, IFAC-PapersOnLine 51 (4) (2018) 119–124, http://dx.doi.org/10.1016/j.ifacol.2018.06.058.
[40] P. Pounds, R. Mahony, P. Corke, Modelling and control of a large quadrotor robot, Control Eng. Pract. (ISSN: 0967-0661) 18 (7) (2010) 691–699, http://dx.doi.org/10.1016/j.conengprac.2010.02.008, URL https://www.sciencedirect.com/science/article/pii/S0967066110000456, Special Issue on Aerial Robotics.
[41] K.L. Shenoy, M.S. Kumar, Design topology and electromagnetic field analysis of permanent magnet brushless DC motor for electric scooter application, in: 2016 International Conference on Electrical, Electronics, and Optimization Techniques, ICEEOT, IEEE, 2016, pp. 1541–1545, http://dx.doi.org/10.1109/ICEEOT.2016.7754942.
[42] H. Suryoatmojo, N. Arsya, R. Mardiyanto, D. Riawan, S.A.M. Ashari, Design of electronic speed controller for BLDC motor based on single ended primary inductance converter (SEPIC), in: 2017 International Seminar on Intelligent Technology and Its Applications, ISITIA, IEEE, 2017, pp. 181–186, http://dx.doi.org/10.1109/ISITIA.2017.8124077.
[43] C.R. Green, R.A. McDonald, Modeling and test of the efficiency of electronic speed controllers for brushless dc motors, in: 15th AIAA Aviation Technology, Integration, and Operations Conference, 2015, p. 3191, http://dx.doi.org/10.2514/6.2015-3191.
[44] V. Nekoukar, N.M. Dehkordi, Robust path tracking of a quadrotor using adaptive fuzzy terminal sliding mode control, Control Eng. Pract. 110 (2021) 104763, http://dx.doi.org/10.1016/j.conengprac.2021.104763.
[45] S. Huang, J. Huang, Z. Cai, H. Cui, Adaptive backstepping sliding mode control for quadrotor UAV, Sci. Program. 2021 (1) (2021) 3997648, http://dx.doi.org/10.1155/2021/3997648.
[46] K. Runcharoon, V. Srichatrapimuk, Sliding mode control of quadrotor, in: 2013 the International Conference on Technological Advances in Electrical, Electronics and Computer Engineering, TAEECE, IEEE, 2013, pp. 552–557, http://dx.doi.org/10.1109/TAEECE.2013.6557334.
[47] M. Herrera, W. Chamorro, A.P. Gómez, O. Camacho, Sliding mode control: An approach to control a quadrotor, in: 2015 Asia-Pacific Conference on Computer Aided System Engineering, IEEE, 2015, pp. 314–319, http://dx.doi.org/10.1109/APCASE.2015.62.
[48] S. Vaidyanathan, C.H. Lien, Applications of Sliding Mode Control in Science and Engineering, vol. 709, Springer, 2017, http://dx.doi.org/10.1007/978-3-319-55598-0.
[49] I. Ahmad, M. Liaquat, F.M. Malik, H. Ullah, U. Ali, Variants of the sliding mode control in presence of external disturbance for quadrotor, IEEE Access 8 (2020) 227810–227824, http://dx.doi.org/10.1109/ACCESS.2020.3041678.
[50] Y. Shtessel, C. Edwards, L. Fridman, A. Levant, et al., Sliding Mode Control and Observation, vol. 10, Springer, 2014, http://dx.doi.org/10.1007/978-0-8176-4893-0.
[51] S. Ullah, A. Mehmood, Q. Khan, S. Rehman, J. Iqbal, Robust integral sliding mode control design for stability enhancement of under-actuated quadcopter, Int. J. Control. Autom. Syst. 18 (2020) 1671–1678, http://dx.doi.org/10.1007/s12555-019-0302-3.
[52] J.S. Bulhões, C.L. Martins, C. Hansen, M.R. da Cunha Reis, A. da Silva Magalhães, A.P. Coimbra, W.P. Calixto, Platform and simulator with three degrees of freedom for testing quadcopters, Robot. Auton. Syst. (ISSN: 0921-8890) 176 (2024) 104682, http://dx.doi.org/10.1016/j.robot.2024.104682, URL https://www.sciencedirect.com/science/article/pii/S0921889024000654.
[53] J. Cacace, V. Scognamiglio, F. Ruggiero, V. Lippiello, Motor fault detection and isolation for Multi-Rotor UAVs based on external Wrench estimation and recurrent deep neural network, J. Intell. Robot. Syst. 110 (4) (2024) 148, http://dx.doi.org/10.1007/s10846-024-02176-2.
[54] A. Altinors, F. Yol, O. Yaman, A sound based method for fault detection with statistical feature extraction in UAV motors, Appl. Acoust. 183 (2021) 108325, http://dx.doi.org/10.1016/j.apacoust.2021.108325.
[55] A. Ferraro, Fault detection and reconfiguration strategies for quadcopter drones deployed in disaster scenarios, in: 2023 IEEE International Workshop on Technologies for Defense and Security (TechDefense), IEEE, 2023, pp. 28–33, http://dx.doi.org/10.1109/TechDefense59795.2023.10380877.
[56] J.S. Bulhoes, C.L. Martins, A.S. Magalhães, A.P. Coimbra, W.P. Calixto, Sliding mode control applied to the stabilization of quadcopters during failures in one of the propulsors, Code Ocean. (2024) http://dx.doi.org/10.24433/CO.3597880.v1.
[57] G. Özdoğan, K. Leblebicioğlu, Design, modeling, and control allocation of a heavy-lift aerial vehicle consisting of large fixed rotors and small tiltrotors, IEEE/ASME Trans. Mechatronics 27 (5) (2022) 4011–4021.
[58] E. Saif, İ. Emınoğlu, Hybrid power systems in multi-rotor UAVs: A scientific research and industrial production perspective, IEEE Access 11 (2022) 438–458.
[59] M. Saied, H. Shraim, C. Francis, A review on recent development of multirotor UAV fault-tolerant control systems, IEEE Aerosp. Electron. Syst. Mag. 39 (9) (2023) 146–180.
[60] L. Dimitri, J. Liscouët, Optimizing flight control of unmanned aerial vehicles with physics-based reliability models, in: 2023 IEEE International Conference on Prognostics and Health Management, ICPHM, IEEE, 2023, pp. 265–273.
[61] M. Gołąbek, M. Welcer, C. Szczepański, M. Krawczyk, A. Zajdel, K. Borodacz, Quaternion attitude control system of highly maneuverable aircraft, Electronics 11 (22) (2022) 3775.
[62] J. Pliego-Jiménez, Quaternion-based adaptive control for trajectory tracking of quadrotor unmanned aerial vehicles, Internat. J. Adapt. Control Signal Process. 35 (5) (2021) 628–641.

Júnio Santos Bulhões Holds a Ph.D. in Control Systems from the Federal University of Goias and an M.Sc. in System Identification. He is a professor at the Federal Institute of Mato Grosso, focusing on control systems and automation, with a focus on developing robust control strategies for industrial processes.

Cristiane Lopes Martins Holds a B.Sc. in Control and Automation Engineering from Federal Institute of Mato Grosso and a post-graduate degree in Software Engineering. She is currently pursuing a master's in Intellectual Property and Technology Transfer for Innovation.

Viviane Margarida Gomes Pacheco Holds a Ph.D. in Systems Complexity from the Federal University of Goias, with research conducted at Carleton University, Canada. She is a professor at the Federal Institute of Goias, with expertise in innovation, intellectual property, systems complexity, and computational intelligence.

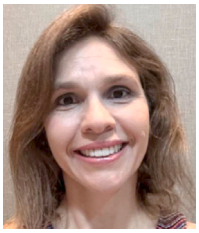

Alana Silva Magalhães Holds a Ph.D. in Electrical Engineering from the Federal University of Goias, with a research period at Carleton University, Canada. She is a professor at the Federal Institute of Goias, specializing in renewable energy, energy efficiency, and electrical power systems.

Clóves Gonçalves Rodrigues Holds a Ph.D. in Physics from UNICAMP, with a postdoctoral fellowship from the same institution. He is a full professor at PUC-GO, collaborating with the Joint Institute for Nuclear Research in Moscow. His research interests include production engineering and systems.

António Paulo Mendes Breda Dias Coimbra Holds a Ph.D. in Electrical Engineering from the University of Coimbra and is an Assistant Professor at the same institution. His research focuses on biped robots, hyper-redundant robots, and electromagnetic compatibility.

Wesley Pacheco Calixto Holds a Ph.D. in Electrical Engineering from the Federal University of Uberlândia, with research conducted at the University of Coimbra. He specializes in system modeling, intelligent systems, and artificial intelligence. Currently, he is a professor at the Federal Institute of Goias and the Federal University of Goias.